ELSEVIER

Contents lists available at ScienceDirect

# **Energy Storage Materials**

journal homepage: www.elsevier.com/locate/ensm





# Nanosecond laser lithography enables concave-convex zinc metal battery anodes with ultrahigh areal capacity

Zechuan Huang <sup>a</sup>, Haoyang Li <sup>b</sup>, Zhen Yang <sup>b,\*</sup>, Haozhi Wang <sup>a</sup>, Jingnan Ding <sup>a</sup>, Luyao Xu <sup>c</sup>, Yanling Tian <sup>d</sup>, David Mitlin <sup>e,\*</sup>, Jia Ding <sup>a,\*</sup>, Wenbin Hu <sup>a</sup>

- <sup>a</sup> Key Laboratory of Advanced Ceramics and Machining Technology (Ministry of Education), School of Materials Science and Engineering, Tianjin University, Tianjin 300072. China
- <sup>b</sup> School of Mechanical Engineering, Tianjin University, Tianjin 300072, China
- <sup>c</sup> Shenzhen Zhongwu Technology Co., Ltd., Shenzhen 518052, China
- <sup>d</sup> School of Engineering, University of Warwick, Coventry CV4 7AL, UK
- e Materials Science Program & Texas Materials Institute, The University of Texas at Austin, Austin, TX 78712-1591, USA

#### ARTICLE INFO

# Keywords: Aqueous zinc batteries (AZB) Zinc dendrites Laser processing Aqueous electrolyte battery Density functional theory (DFT)

#### ABSTRACT

Laser processing is employed to fabricated zinc-ion battery (ZIB) anodes with state-of-the-art electrochemical performance from commercial zinc foils. Lasers are widely utilized for industrial surface finishing but have received minimal attention for zinc surface modification. Laser lithography patterned zinc foils "LLP@ZF" are hydrophilic, with an electrolyte contact angle of  $0^{\circ}$ . This is due to the concave-convex surface geometry that enhances wetting (periodic crests, ridges and valleys, roughness 16.5 times planar). During electrodeposition LLP@ZF's surface geometry generates a periodic electric field and associated current density distribution that suppresses tip growth (per continuum simulations). Per Density Functional Theory (DFT) its surface oxide is zincophilic, resulting in low nucleation barriers during plating (e.g. 3.8 mV at 1 mA cm $^{-2}$ ). A combination of these attributes leads to stable dendrite-free plating/stripping behavior and low overpotentials at fast charge (e.g. 48.2 mV at 8 mA cm $^{-2}$  in symmetric cell). Cycling is possible at an unprecedented areal capacity of 50 mA h cm $^{-2}$ , with 400 h stability at 1 mA cm $^{-2}$ . Moreover, exceptional aqueous zinc battery (AZB) performance is achieved, with MnO<sub>2</sub>-based cathode loading 10 mg cm $^{-2}$  and corresponding anode capacity 7.6 mA h cm $^{-2}$ . A broad comparison with literature indicates that LLP@ZF symmetric cell and full battery performance are among most favorable.

# 1. Introduction

The global economy is rapidly electrifying, and in the process coming closer to carbon dioxide neutrality while reducing overall environmental pollution [1–3]. Although lithium-ion batteries (LIBs) will remain dominant for vehicular and portable energy storage applications, there is a motivation to develop less-expensive and safer aqueous systems for stationary energy storage [4–7]. Aqueous electrolytes possess the advantages of non-flammability and low cost as compared with organic electrolytes [8–10]. Aqueous zinc batteries (AZBs), including Zn-Air battery [11], Zn-Mn battery [12], Zn-Ni battery [13], Zn-chalcogen battery [14] are being considered for non-vehicular end uses. Metallic zinc is regarded as one of the most promising aqueous battery anodes, being abundant in the earth's crust (about 75 ppm),

possessing a high theoretical capacity (820 mA h g $^{-1}$ ) and low electrochemical potential (-0.76 V vs. SHE) [15,16]. The stability of Zn in air and its mechanical formability allows for large-scale production of commercial AZBs [17,18].

Many challenges for the key electrode and electrolyte materials still obstruct the practical applications of AZBs. As the universal negative electrodes for all types of AZBs, the cycling instability of the zinc metal anode is a key bottleneck [19–22]. A major issue for the zinc anode is the uncontrollable electrodeposition leading to the formation of dendrites [23,24]. While not being a fire risk, Zn dendrite formation nevertheless limits the lifetime and commercial viability of AZBs. It is well demonstrated that zinc dendrite formation impairs the kinetics of zinc plating, resulting rapid decline in capacity and cycling performance [25,26]. After repeated metal plating/stripping, the dendrites may detach from

E-mail addresses: yangzhen1992@tju.edu.cn (Z. Yang), david.mitlin2@utexas.edu (D. Mitlin), jiading@tju.edu.cn (J. Ding).

<sup>\*</sup> Corresponding authors.

zinc foils. Fresh metallic zinc exposed to the electrolyte enhances the corrosion side reactions, which deteriorates the Coulombic efficiency (CE) of AZBs [27].

Numerous innovative strategies have been attempted reduce the zinc dendrite issue, aiming at optimizing the zinc electroplating/striping behavior [28-45]. The electrodeposition of metallic zinc is essentially controlled by the mass and electron transfer processes at the zinc anode/electrolyte interface. The ion flux and the local electric fields at the vicinity of zinc anode significantly influence the zinc nucleation and the subsequent crystal growth [28-31]. Introducing heterogeneous porous passive layers on zinc anode has been demonstrated to be an effective way to achieve uniform zinc electrodeposition [32,33]. Various electrolyte additives have been demonstrated to be effective in suppressing dendrites [34,35]. Areal current density is another crucial aspect determining dendritic versus dendrite-free growth. It is known that a high current density promotes dendrite nucleation at the expense of a planar front achieved at lower currents [36,37]. Artificially introducing heterogeneous nucleation sites with high zinc affinity has been demonstrated as effective for dendrite-free zinc plating and stripping [37,38]. Structure engineered zinc anodes and current collectors with three-dimensional geometries have been demonstrated to reduce the effective current density and promote ion diffusion thereby favoring uniform zinc deposition [39-42]. For example, Duan's group conducted inspiring studies on fabricating high-perform 3D structured zinc anodes via advanced micromanufacturing methodologies [43-45]. The novelty in the current approach is the use of laser lithography to obtain a periodic concave-convex geometry with state-of-the-art electrochemical performance, which has not been done previously. To date, considerable progress has been achieved to enhance the zinc anode performance. Nonetheless, it is still challenging to fabricate advanced zinc anodes by existing manufacturing procedures. Equally importantly there is lack of zinc anodes that can stably cycled at practical areal capacities, for example higher than 5 mA h cm<sup>-2</sup>. New methodologies for scalable fabrication of zinc anodes with high areal capacity are therefore needed to further advance AZBs.

Here, we tuned an established metallurgical surface finishing method based on laser processing to fabricate a periodic concave-convex (egg crate -like geometry) patterned zinc anode from commercial zinc foils. The resultant unique zinc anode architecture is termed Laser Lithography Patterned Zinc Foils (LLP@ZF). Laser lithography is an industrial process for surface modification of metals, additive manufacturing, and micromachining [46–48]. However, it has never been applied to structuring of Zn foils in any context and holds promise in its scalability and industrial utility. Due to the advantage of being already established for other industrial uses, the laser approach is ideally suitable for scalable zinc electrode manufacturing. It is demonstrated that the unique attributes of LLP@ZF include surface chemistry-induced zincophilicity and geometry-induced hydrophilicity. Combined these two attributes allow for facile and cyclically stable metal anode plating/stripping kinetics and state-of-the-art full battery performance.

## 2. Experimental section

# 2.1. Zinc anode fabrication

Laser Lithography Patterned Zinc Foils, termed LLP@ZF, were used as the target electrodes. Two baselines were also fabricated and tested. As the first baseline, washed zinc foils were analyzed, being termed bare ZF. The second baseline, termed ZnO@ZF, was obtained by annealing bare ZF at 250°C in air atmosphere for 1 h. This specimen was employed for evaluating the role of ZnO layer on zinc foils while excluding the geometrical morphology effect. Prior to the laser lithography procedure, the commercial zinc foils were ultrasonically washed with acetone, followed by ethanol, and distilled water so as to remove residual organics from the surface. The polished zinc foils were dried by compressed nitrogen and employed directly for laser lithography. The type

of laser utilized is a nanosecond Ytterbium fiber laser source (IPG photonics from Germany) with a wavelength ( $\lambda$ ) of 1064 nm, pulse duration ( $\tau$ ) of 50 ns and repetition rate (f) up to 20 kHz. The selected output power (P) was 12 W. The spot diameter ( $\Phi$ ) and the focal length of the lens were set to 50  $\mu$ m and 182 mm, respectively, at each ablation step. The distance (S) between adjacent laser scanning lines was 100  $\mu$ m in x and y directions, this resulting in the micron-scale periodical concave-convex pattern on the ablated surface.

#### 2.2. Material characterization

Analysis of the surface morphology was obtained by scanning electron microscopy SEM (JSM-7800F). 3D height profiles were obtained by light optical microscopy, using a white confocal light microscope (CountourGT, Bruker). Crystal structure information was obtained by X-ray diffraction XRD (Bruker D8 ADVANCE). Surface chemistry and bonding analysis was obtained by X-ray photoelectron spectroscopy XPS (KratosAxis Supra). Static contact angle analysis between the electrolyte (2 M ZnSO<sub>4</sub> aqueous solution) and the electrodes was performed using a drop shape analyzer (JY-82B Kruss).

#### 2.3. Electrochemical measurements

The symmetric cells were assembled using LLP@ZF, baseline ZnO@ZF, or baseline bare ZF specimens. For the asymmetric cells, Cu foils were used as positive electrodes opposing LLP@ZF, ZnO@ZF and bare ZF. The aqueous solution of 2 M ZnSO<sub>4</sub> was used as the electrolyte for symmetric and asymmetrical cells. Glass fiber membranes (GF/C) were employed as separators in all cases. For the full cells, MnO2 cathodes and zinc metal anodes were assembled into 2032 coin cells with 2 M  $ZnSO_4 + 0.1$  M  $MnSO_4$  aqueous electrolyte. Glass fiber membranes were employed as separators. MnO2 cathode material was synthesized through a hydrothermal method [49]. The fabricated MnO<sub>2</sub> powder, carbon nanotubes and PVDF, with a ratio of 7:2:1, was mixed in NMP to obtain a well-dispersed slurry. The slurry was then coated on the carbon paper (1 cm<sup>2</sup>) and dried at 60°C overnight. The mass loading of cathodes was ca. 1 mg cm<sup>-2</sup>. Cyclic voltammetry (CV) and electrochemical impedance spectroscopy (EIS) were obtained using a Solartron 1470E analytical workstation. Galvanostatic charge-discharge tests were carried out using a LAND CT2001A.

#### 3. Results and discussion

Fig. 1(a) illustrates the top-down fabrication process of the geometrically periodic concave-convex Laser Lithography Patterned Zinc Foils (LLP@ZF) by nanosecond laser lithography. The laser lithography process was performed on commercial zinc foils. The unprocessed zinc foils were also tested as a baseline, being termed "bare ZF". In summary, zinc foils are ablated in a periodic manner (line-byline) in ambient atmosphere using a nanosecond Ytterbium fiber laser source (the wavelength of 1064 nm). The distance between the parallel ablation lines is set to be 100  $\mu m$ . After the ablation along one direction there is a subsequent ablation in the perpendicular direction, this generating the targeted periodic concave-convex pattern. The processing efficiency of this laser lithography process is 1 m<sup>2</sup> per hour for the LLP@ZF product. Fig. 1(a) also shows two examples of LLP@ZF electrodes, one fabricated to  $1 \times 1$  cm and one fabricated to  $10 \times 10$  cm. Both were made in an identical manner, with size of the processed foil being computer controlled.

Scanning electron microscopy (SEM) and confocal light optical microscope-obtained three-dimension (3D) surface topography were utilized to investigate the morphology LLP@ZF. The periodic patterned egg crate - shaped concave-convex surface can be observed in Fig. 1(b). The surface topography in Fig. 1(c) reveals that the pattern displays well-defined crests (red), ridges (green) and valleys (blue). The interval between adjacent crests and between adjacent valleys is  $100~\mu m$ , in line

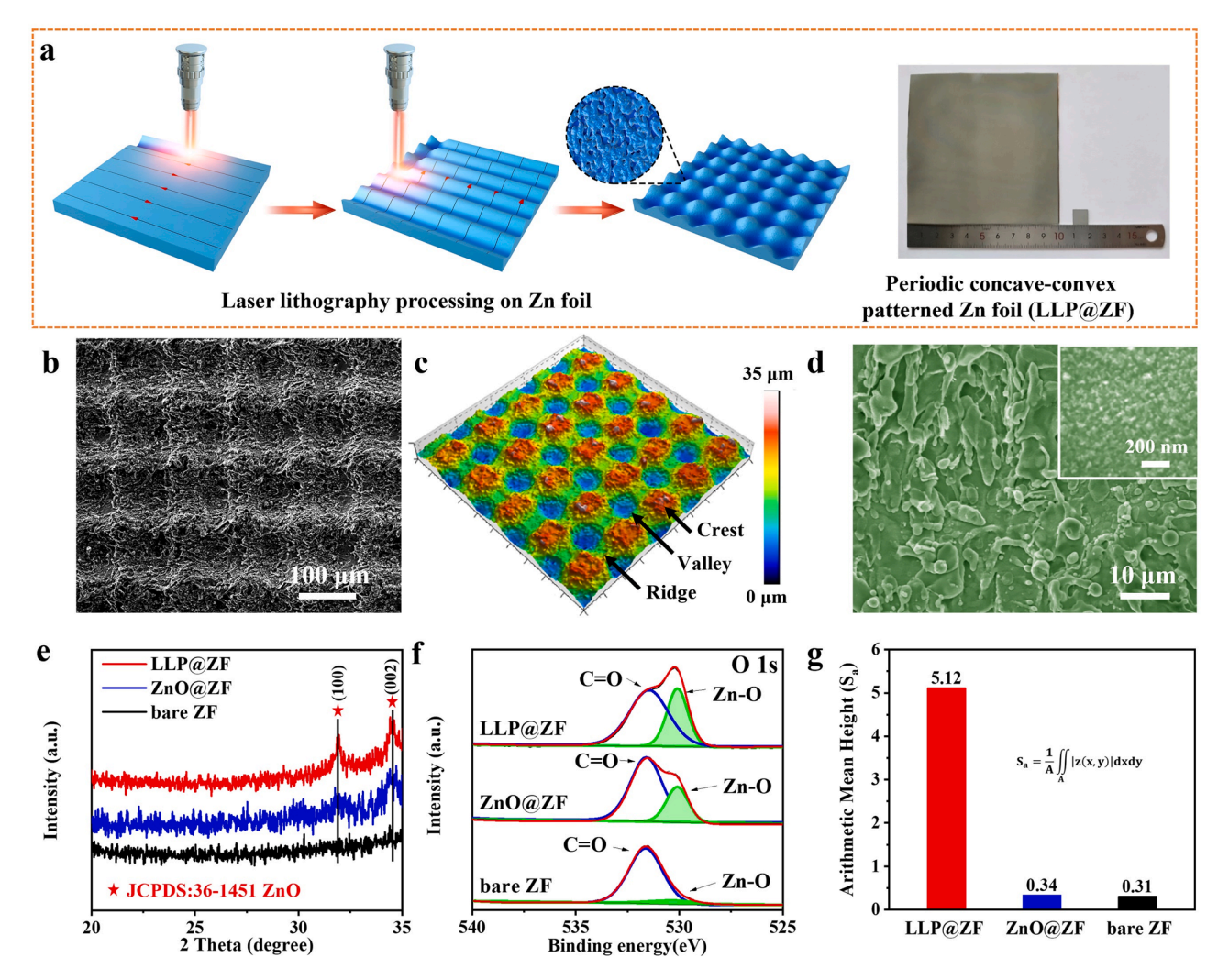


Fig. 1. (a) (left) Schematic illustrating the top-down fabrication process of the geometrically periodic concave-convex Laser Lithography Patterned Zinc Foils (LLP@ZF) by nanosecond laser lithography. (right) Two identical LLP@ZF electrodes cut to a different size. (b),(c),(d) Low magnification SEM image, confocal light microscope map, and higher resolution SEM image of the LLP@ZF surface. (e),(f),(g) Indexed XRD patterns, high resolution XPS O 1s spectra and Arithmetical Mean Height (S<sub>a</sub>) bar chart obtained from the confocal light microscope images. Analysis performed on LLP@ZF, baseline ZnO@ZF and baseline bare ZF.

with the selected laser lithography parameters. The average height difference between crests and valleys is 22  $\mu m$ . This is indicated by the height profile of LLP@ZF, shown in Fig. S1. The SEM images in Fig. 1(d) and in Fig. S2 demonstrate the inherently finer-scale secondary roughness of the lasered surfaces. This secondary roughness is consistent from region to region, being a combination of micron-scale and nanoscale. It is associated with localized melting and evaporation of the Zn during lasering.

In addition to the LLP@ZF sample, two reference samples were also prepared and analyzed. As already mentioned, one baseline is the pristine Zn foil termed "bare ZF". As shown in Fig. S3(a)-(b), bare ZF displays a relatively flat surface, except for a few pits that appear as black dots. To further analyze the role of the surface oxide in electrolyte wetting and metal nucleation, a Zn foil was annealed at 250°C in air to obtain "ZnO@Zn" baseline. According to the SEM images in Fig. S3(c)-(d), there are no obvious changes in the macroscopic foil geometry after the anneal. However, the grown ZnO layer displays relatively loose and porous morphology. The elemental composition of electrode surfaces was analyzed using SEM Energy Dispersive X-ray Spectroscopy (EDXS). As shown in Fig. S2, the crest, ridge and valley regions of LLP@ZF yield an oxygen content of 18.2, 22.6 and 25.2 wt%, respectively. Because the SEM electron beam possesses a relatively large interaction volume these numbers reflect signal not only the surface oxide but also from the

underlying pure Zn metal. According to Fig. S3, the ZnO@ZF exhibits an oxygen content of 13.2 wt%, which is also a balance of the signal from the surface oxide and from the underlying metal. For bare ZF, the oxygen content is at 5.3 wt%, indicating an overall thinner oxide layer. The full-range X-ray powder diffraction (XRD) patterns of bare ZF and LLP@ZF are shown in Fig. S4. The Bragg peaks of the metallic zinc can be indexed for all three samples. As shown in Fig. 1(e), the (100) and (002) Bragg peaks at 31.8° and 34.4° corresponding to the hexagonal ZnO phase (P63mc) are distinctly visible in the LLP@ZF and ZnO@ZF patterns. The bare ZF is covered by a sufficiently thick surface product that the Bragg peaks are less discernable.

X-ray photoelectron spectroscopy (XPS) was used to further analyze the surface chemistry and bonding in the three specimens. Per Fig. 1(f), the O1s spectra of LLP@ZF and ZnO@ZF can be deconvoluted into two peaks at 529.8 eV and 531.4 eV, which are ascribed to the binding energies of Zn-O and C=O, respectively [50]. By contrast, the Zn-O peak intensity for bare ZF is very weak. Instead, the C=O signal observed in O 1s is due to the passivating layer of basic zinc carbonate  $(Zn_5(OH)_6(CO_3)_2)$ . The carbonate is accepted to be the terminating structure of standard zinc metal surfaces in contact with an ambient environment [51,52]. The carbonate layer is likely amorphous, which explains the lack of structure in the XRD pattern. As shown by the TEM analysis in Fig. S5(a), the LLP@ZF surface displayed polycrystalline ZnO

and Zn phases. Per the high-resolution TEM image of LLP@ZF shown in Fig. S5(b), the typical crystallite size is determined to be in the 10 nm range. The associated SAED ring patterns indicate no preferential texture for either Zn or ZnO. For the baseline bare Zn, the individual diffraction spots in the selected-area electron diffraction pattern (SAED) indicate that the grain size is on the order of microns and is not random.

It is expected that rolled metallurgical foils will have a strong <001> fibre texture rather than random grain orientation [53]. Those results are shown in Fig. S5(c),(d).

The crystallite sizes for bare ZF are substantially larger than that of LLP@ZF. This indicates that the lasering process induces recrystallization (from solid, melt and/or vapor) in the zinc foil. It is known that the

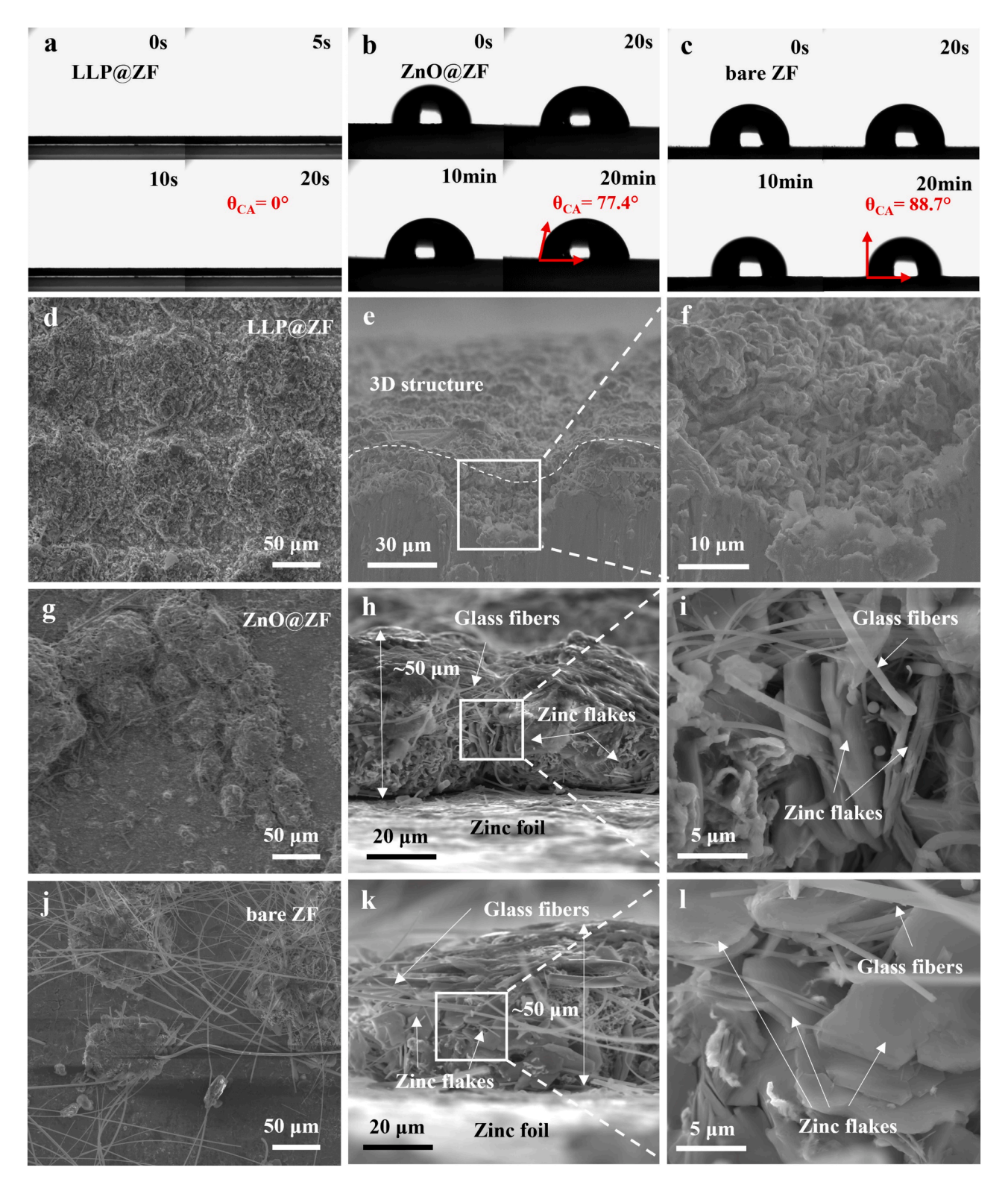


Fig. 2. (a)–(c) Optical images of the 2 M ZnSO<sub>4</sub> electrolyte – electrode contact angles, comparing LLP@ZF versus baseline ZnO@ZF and baseline bare ZF. (d)-(l) Top view and cross-sectional view SEM images highlighting the surface morphology of the three electrodes, with zinc electrodeposited capacity of 2 mA h cm $^{-2}$  at 0.5 mA cm $^{-2}$ .

electrochemically driven nucleation of zinc is closely related to the crystallographic texture and grain size of the zinc anode [54,55]. Due to epitaxial growth, a smaller grain size in the underlying metal will lead to a smaller grain size in the plated deposit. This will smoothen the surface and reduce the likelihood of large individual or agglomerated zinc flakes (crystallites). During the lasering process, the ablated metal adsorbs a tremendous amount of heat, becoming locally molten and evaporated [56–58]. Superheated liquid droplets are ejected into the air above the metal surface, undergoing rapid cooling as gravity brings them back in contact with the foil. This, combined with more complex events including a laser-induced plasma plume, results in the secondary microscale and nanoscale roughness observed on the LLP@ZF surface. As the surface is solidified but remains hot, the ZnO layer is spontaneously formed due to the presence of water vapor in contact with the metal. However this newly formed surface oxide remains fairly thin due to the rapid cooling kinetics [59,60].

To quantify the degree of macroscopic roughness of the anodes, the Arithmetical Mean Height S<sub>a</sub> was calculated for the three specimens. The confocal light optical microscope images were employed for the calculation. S<sub>a</sub> is an absolute value which expresses the difference in height of each point as compared to the arithmetical mean of the surface. The equation for calculating S<sub>a</sub> is shown in the inset of Fig. 1(g), Per Fig. 1(g), Sa for bare ZF is 0.30 μm, indicating a relatively smooth surface. The LLP@ZF specimen has S<sub>a</sub> of 5.12 μm, which is 16.5 times of baseline ZF. The direct oxidation of ZF surface made only minimal change to its macroscopic surface roughness, Sa being 0.34 µm for ZnO@ZF. The electrochemical surface area is another method to evaluate the roughness of a given surface. Cyclic voltammetry (CV) tests based on symmetric cells were conducted to estimate the surface area. The electrolyte employed was 2 M ZnSO<sub>4</sub> aqueous, which is the same as for the symmetric cells. The analysis assumes that the integral area of the CV curve is proportional to the active surface area of the electrode [61,62]. As shown in Fig. S6, LLP@ZF displays an integrated area that is 8 and 15 times higher than that of ZnO@ZF and bare ZF, respectively.

The LLP@ZF specimen is hydrophilic, allowing for complete wetting by the electrolyte. As shown in Fig. 2(a), the electrolyte wetted the LLP@ZF surface in less than one second, resulting in a contact angle of 0°. By contrast the same electrolyte poorly wets the bare ZF surface. The contact angle between the electrolyte and bare ZF is measured to be 88.7°, the high wetting angle indicating hydrophobicity. The ZnO@ZF surface gives a contact angle of 77.4°. The surface tension of ZnO and Zn was calculated by Density Function Theory (DFT). As shown in Table S1, the surface tension of ZnO (002) and (101) planes are 1.54 N m $^{-1}$  and 2.34 N m $^{-1}$ , respectively. These tensions are more than twice as high as those calculated for pure Zn (002) and (101), being 0.53 N m $^{-1}$  and 1.07 N m $^{-1}$ , respectively. Based on these differences, ZnO should be more hydrophilic than metallic zinc (liquid-vapor surface tension should be the same in each case).

According to classical Wenzel theory, an increase of surface roughness has an amplification effect for surface wettability [63,64]. Surface roughness can either promote enhanced wetting or vise-versa promote enhanced dewetting as compared to perfectly planar surface. Weakly hydrophilic surfaces can become strongly hydrophilic, while weakly hydrophobic surfaces can become strongly hydrophobic. The point may be illustrated by modifying the Young's equation to be in units of force, rather than in customary units of force per length: The substrate surface area is defined as  $S_a$ . Then  $S_a^{0.5} \gamma_{sl} + \gamma_{lv} \cos\theta = S_a^{0.5} \gamma_{sv}$ , where  $\gamma_{sl}$  is the solid - liquid tension,  $\gamma$ lv is the liquid - vapor tension, and  $\gamma$ sv is the solid - vapor tension. This approach is approximate since assumes the available surface area is perfectly wetted. However, it remains instructive in understanding the role of surface roughness in affecting the wetting behavior. It may be observed that increased substrate roughness has an asymmetrical effect, not influencing the liquid - vapor tension where the higher substrate surface area plays no role. Given the similar roughness of ZnO@ZF and bare ZF, the greater hydrophilicity of ZnO@ZF over bare ZF is driven by the improved intrinsic wetting due to the ZnO. The major

enhancement in hydrophilicity with LLP@ZF is then attributed to its roughness that amplifies the benefit from the oxide.

Zinc plating behavior of the LLP@ZF and baseline bare Zn and ZnO@ZF electrodes was firstly investigated using a symmetric cell configuration. Fig. 2(d)-(f) show the morphology of LLP@ZF surface after 2 mA h cm $^{-2}$  of plated capacity (not cycled), deposited at 0.5 mA cm<sup>-2</sup>. It may be observed that the zinc surface maintains its pre-existing concave-convex morphology, with no evidence of isolated islands of the plated metal. By contrast, zinc deposition is non-uniform on the ZnO@ZF and bare Zn surfaces. Fig. 2(g)-(i) show the morphology of ZnO@ZF surface with 2 mA h cm<sup>-2</sup> of plated zinc capacity, also deposited at 0.5 mA cm<sup>-2</sup>. It may be observed that the zinc surface is irregular in morphology. In addition, regions of pristine zinc foil surface absent of plated zinc are discernable. Rather than depositing as a blanket film, plated zinc assumes the form of islands. The islands are in-turn composed of aggregates of plate-shaped crystal flakes along with oxidation products and imbedded glass fit fibers from the separator. It is not feasible to extract the post-cycled anode without the inclusion of the glass frit. For clarity, the glass fibers are labeled in several of the SEM images throughout the manuscript. The zinc flakes are observed in cross sectional view of SEM images, being a typical morphology of zinc deposits in ZnSO<sub>4</sub> electrolytes [65,66]. Similar isolated zinc island full of glass fibers and corrosion products are observed on the bare Zn surfaces, per Fig. 2(j)-(l). Although some fibers are also imbedded in plated surface of LLP@ZF, this occurs to a significantly lesser extent. Analogous zinc metal – glass fiber networks have been reported previously [67].

Without complete wetting of the pre-existing metal surface, zinc will not be able to deposit uniformly. Of course, areas not wetted by the electrolyte will remain electrochemically inactive. Since electrolyte wetting of the bare ZF and ZnO@ZF surfaces is incomplete, the wetted regions will experience a true current density that is higher than the nominal. The ionic flux and the electrical field in regions that are locally wetted is expected to be non-uniform. The electrolyte droplet edge effect is a source of flux heterogeneity and electric field focusing. In contrast, the fully wetted surface of LLP@ZF decreases the true current density at the anode due to its enhanced electroactive surface area. This will lead to less concentration polarization for a given nominal current, with any partial-wetting edge effects being eliminated. It may be now concluded that the laser lithography pattern on LLP@ZF plays a vital role in modulating the zinc electrodeposition behavior. The complete electrolyte wetting due to a combination of ZnO and periodic surface roughness. The other key factor that promotes uniform zinc deposition with LLP@ZF is its zincophilicity, which will discussed later in the context of additional DFT simulation results.

Fig. 3(a) displays the initial plating overpotential profiles of the three electrodes, tested at 1 mA cm<sup>-2</sup>. It should be noted that lower currents (typically below 0.5 mA cm<sup>-2</sup>) have been employed for this analysis in prior studies, per Table S2. Therefore, the tests performed here represent an aggressive regiment where dendrite formation is favored with conventional foil geometries. In the profiles, the difference between the peak overpotential and the following stable plating overpotential is the nucleation overpotential [68,69]. At 1 mA cm<sup>-2</sup>, the nucleation overpotential of LLP@ZF is 3.8 mV, versus the 58.6 mV for ZnO@ZF and 99.8 mV for bare ZF. The stable overpotential that follows nucleation corresponds the grain growth stage of the plating process. Repeated zinc plating/striping performance of LLP@ZF, ZnO@ZF and bare ZF anodes was evaluated through galvanostatic cycling of the symmetrical cells at various areal current densities and specific capacities. Fig. 3(b) displays the voltage profiles of symmetric cells with areal capacity of 0.5 mA h cm<sup>-2</sup> at 0.5 mA cm<sup>-2</sup>. For symmetric bare ZF and ZnO@ZF based cells, a sudden voltage drop at 267 h and at 190 h indicates short-circuiting of the cells. As shown in Figs. 3(c) and S7, short-circuit failure is manifested as perfect rectangle voltage profiles with constant miniscule overpotential corresponding to the ohmic loss in the electrically conductive zinc. In contrast, LLP@ZF symmetrical cell delivered stable plating/stripping polarization and lasted for over 1100 h.

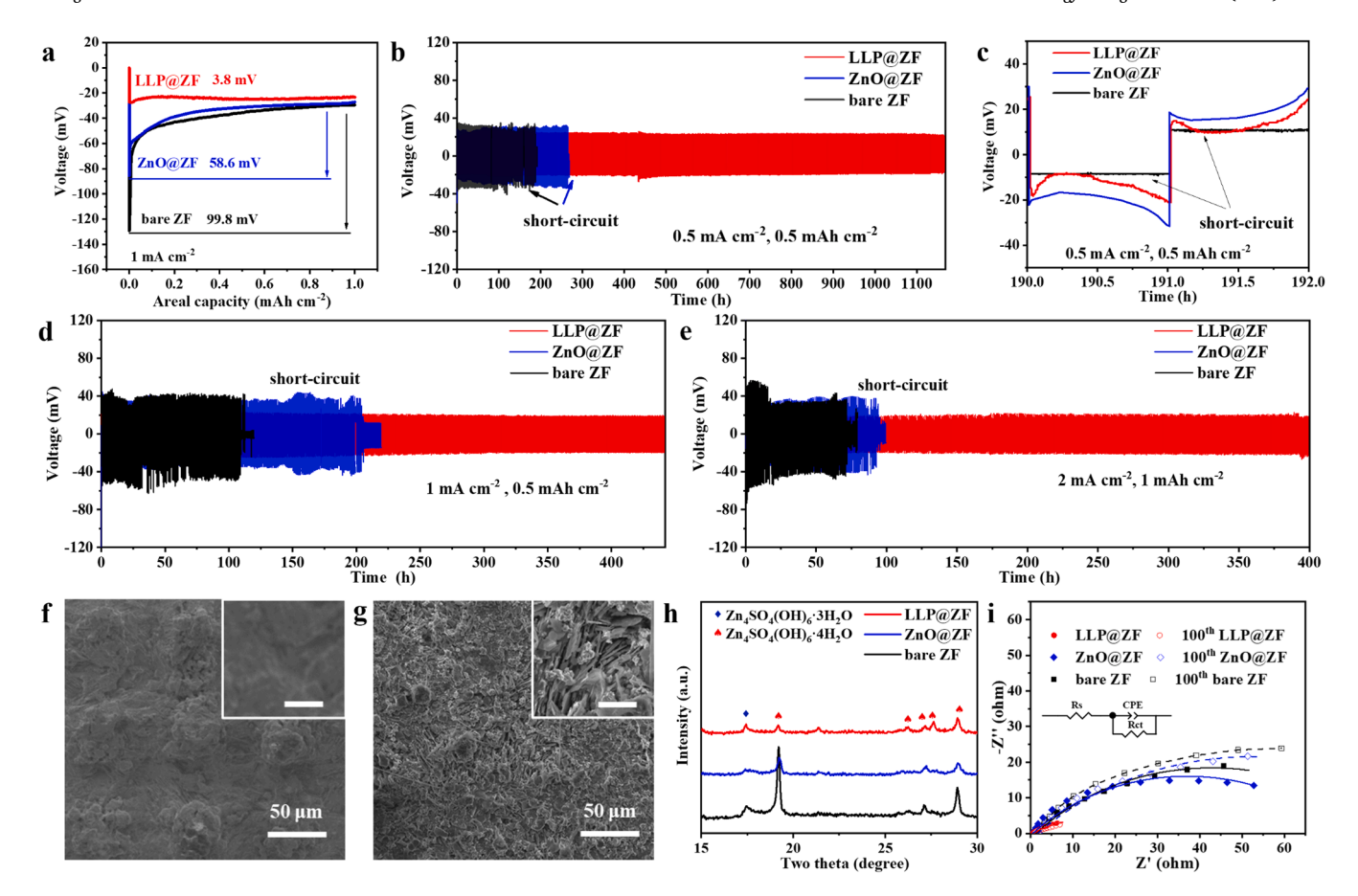


Fig. 3. Voltage profiles of LLP@ZF versus ZnO@ZF and ZF, tested in symmetrical cells in 2 M ZnSO<sub>4</sub> electrolyte. (a) Initial plating voltage profiles of LLP@ZF, ZnO@ZF and bare ZF, tested in symmetrical cells at 1 mA cm<sup>-2</sup> in 2 M ZnSO<sub>4</sub> electrolyte, (b),(c) Voltage profiles tested at 0.5 mA cm<sup>-2</sup> with 0.5 mA h cm<sup>-2</sup> capacity per cycle, (d) Voltage profiles tested at 1 mA cm<sup>-2</sup> with 0.5 mA h cm<sup>-2</sup> capacity, (e) Voltage profiles tested at 2 mA cm<sup>-2</sup> with 1 mA h cm<sup>-2</sup> capacity. (f) Morphology of LLP@ZF after 100 cycles at 1 mA cm<sup>-2</sup> with 0.5 mA h cm<sup>-2</sup> capacity (inset scale bar = 5  $\mu$ m). (g) Analogous analysis for bare ZF. (h) XRD patterns of post-cycled electrodes obtained from symmetrical cells, 100 cycles at 1 mA cm<sup>-2</sup> with 0.5 mA h cm<sup>-2</sup> capacity. (i) Fitted EIS Nyquist plots for the three specimens before and after cycling. (Inset: The fitting circuit model for Nyquist plots in symmetrical cells).

According to Figs. 3(d)-(e) and S8, at higher current densities of 1 and 2 mA cm  $^{-2}$  , the bare ZF cells lasted for  $\bar{113}\,h$  and 75 h before short circuiting. The ZnO@ZF based cells lasted 206 h and 98 h before short circuiting. The LLP@ZF cells maintained stable cycling for 440 h and 400 h at which point the test was concluded. During cycling the cells displayed a stable average polarization at around 23 mV and did not show electrochemical evidence of transient short circuiting. The distinctly improved zinc plating/striping behavior indicates that LLP@ZF has alleviated zinc dendrite growth. To further understand the plating/stripping kinetics, the voltage polarization at different current densities was analyzed. As shown in Fig. S9, significantly lower voltage polarization with LLP@ZF is achieved as compared to bare ZF. For LLP@ZF, the average plating/stripping overpotentials are 20.1, 21.8, 23.7, 38.6 and 48.2 mV when tested at 0.5, 1, 2, 4, 8 mA cm respectively. According to Table S3, the 48.2 mV overpotential at 8 mA  $\mbox{cm}^{-2}$  is among the most favorable reported in literature, considering the relatively high current that was employed.

The mean overpotential values for the ZnO@ZF cell are 30.6, 36.0 and 42.6 mV at 0.5, 1, 2 mA cm $^{-2}$ , respectively. The mean overpotential values for bare ZF are 42.4, 54.2 and 58.7 mV at 0.5, 1, 2 mA cm $^{-2}$ , respectively. The larger overpotentials with both electrodes indicate that nucleation is more difficult, and that island formation is favored per the theoretical analysis put forth in refs [70]. During repeated plating and stripping, the zinc islands grow and shrink. In the processes a higher aspect dendrite morphology is established that ultimately short circuits the symmetric electrodes together. Fig. S9 shows the voltage profiles of LLP@ZF, ZnO@ZF and bare ZF symmetric cells, tested at 0.5, 1, 2, 4 and

8 mA cm $^{-2}$ , increased in a stepwise manner. It may be observed that as the current increased to 4 mA cm $^{-2}$ , the bare ZF cell short-circuited. This agrees with the standard expectation that a high current density accelerates dendrite growth due to electrical field concentration effects at the metal protrusions [71–73].

Coulombic efficiency measurements were conducted by testing LLP@ZF||Cu, ZnO@ZF||Cu and bare ZF||Cu in half-cells. Per Fig. S10 the bare ZF||Cu cell noticeably declined in stability at around 134th cycle, as marked by its rapidly deteriorating CE. The ZnO@ZF||Cu specimen fails in a comparable manner to bare Zn, having its CE rapidly decline after 144 cycles. By contrast, the LLP@ZF||Cu cell maintains stable reversible plating and stripping for 270 cycles. During cycling the LLP@ZF||Cu cell maintains an average CE of 99.5%, indicating minimal parasitic reactions. As shown in Fig. S11, this CE performance is among the most favorable relative state-of-the-art zinc anodes in scientific [26, 41,42,72,74-76].

The post-cycled electrodes were collected from the symmetric cells and analyzed by SEM and confocal light optical microscopy, the results being shown in Figs. 3(f)-(g) and S12. Fig. 3(f) demonstrates that the post-cycled LLP@ZF surface morphology is analogous to its starting morphology. A magnified image in the inset reveals the relatively smooth topography even on the micro-scale. The optical images in Fig. S12(a) demonstrate that the periodic concave-convex pattern remains well maintained. Fig. 3(g) shows the post-cycled bare zinc surface, consisting of island-like deposits that are agglomerates of zinc flakes, corrosion product, and glass fibers. The high resolution inset in the figure illustrates this structure. With near-neutral aqueous

electrolytes "dendrites" consist of micron-scale stacked zinc plates making up larger irregularly shaped protrusions. This morphology agrees well with prior reports for Zn dendrite formation and growth in near-neutral electrolytes, where the structures do not resemble sharp protrusions [77–80]. It is only in alkaline electrolytes does the deposited zinc take on the sharp and often branched features of a classic dendrite [81,82]. The confocal images of the post cycled bare Zn surface, shown in Fig. S12(b) further demonstrate the specimens surface roughness. Similar morphology was also observed for post cycled ZnO@ZF electrode, per Fig. S13.

After 100 cycles, corrosion products ascribed to  $\rm Zn_4(OH)_6SO_4\cdot 3H_2O$  and  $\rm Zn_4(OH)_6SO_4\cdot 4H_2O$  were detected on all three electrodes, per Fig. 3 (h). This agrees with prior reports for reaction of Zn anodes in sulfate electrolytes [83,84]. However the relative peak intensity of the products with ZnO@ZF and LLP@ZF is significantly lower than with bare ZF, which supports the role of ZnO in protecting the metal. Fig. S15 shows the morphologies and elemental analysis for the three electrodes after one complete zinc plating/stripping process. The ZnO@ZF and bare ZF

displayed 20 micrometer-scale pits throughout its surface, which were absent in the LLP@ZF specimen. The sulfur content on the electrodes' surface after one cycle was employed as an additional corrosion indicator. Per EDXS analysis, bare ZF yielded a sulfur content of 5.7 wt%, ZnO@ZF yielded 1.6 wt%, while LLP@ZF yielded 2.3 wt%, respectively.

Static surface corrosion of the anodes was investigated by soaking them in the same electrolyte solution for five days. As shown in Fig. S16, the initially smooth surface of the bare ZF was replaced by a rough surface covered by corrosion pits and by-products, indicating that the native carbonate-terminating surface is not stable. By contrast, the surface morphology of LLP@ZF and ZnO@ZF did not display noticeable changes, indicating that the ZnO is relatively stable. Tafel curves were employed to further evaluate the corrosion rate of the three anodes, the results being plotted in Fig. S16(d). Bare ZF displayed a current of 3.5  $\times$   $10^{-3}$  A cm $^{-2}$ , as compared to 2.7  $\times$   $10^{-3}$  A cm $^{-2}$  for LLP@ZF and 2.5  $\times$   $10^{-3}$  A cm $^{-2}$  for ZnO@ZF. These results confirm the benefit of ZnO versus a native carbonate-terminated surface.

Fig. 3(i) shows the electrochemical impedance spectra (EIS) of

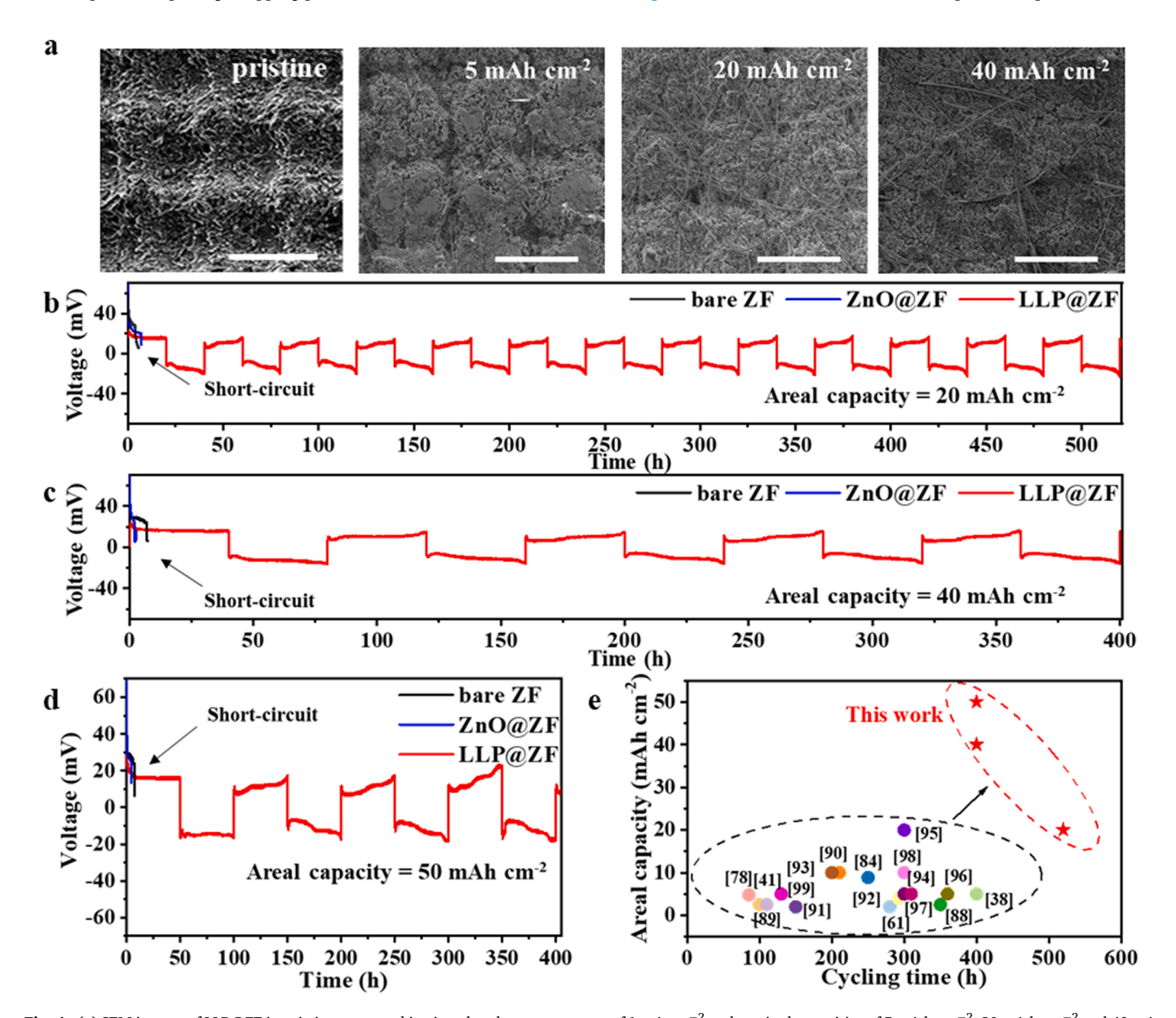


Fig. 4. (a) SEM images of LLP@ZF in pristine state, and in zinc plated state at current of 1 mA cm $^{-2}$  to deposited capacities of 5 mA h cm $^{-2}$ , 20 mA h cm $^{-2}$  and 40 mA h cm $^{-2}$ , respectively (Scale bar: 100  $\mu$ m). (b) – (d) Voltage profiles of symmetrical cells of LLP@ZF, ZnO@ZF or bare ZF, cycled at 1 mA cm $^{-2}$  to an areal capacity per cycle of 20 mA h cm $^{-2}$ , 40 mA h cm $^{-2}$  and 50 mA h cm $^{-2}$ . (e) A comparison of areal capacity and cycling time of LLP@ZF with the-state-of-the-art Zn metal anodes from literature.

electrodes at the pristine and post-cycled (100 cycles) states. The tested frequency range employed is from 100,000 Hz to 0.01 Hz. The data were fitted based on the equivalent circuit shown in the inset. The absence of a Warburg component agrees with zinc metal anode literature [31,85]. Initially, the charge transfer resistance of the symmetrical cell based on LLP@ZF was 21.7  $\Omega$ , versus 102.3  $\Omega$  for bare ZF and 72.4 $\Omega$  for ZnO@ZF. Reduced charge transfer resistance has been attributed to improved electrolyte wetting and enhanced zincophilicity of the surface [31,86], and agrees with previously discussed wetting results. After cycling, the charge transfer resistance with LLP@ZF remains stable at 23.2  $\Omega$ , while with bare ZF and ZnO@ZF it increases incrementally to 123.4  $\Omega$  and 112.8  $\Omega$ . A cycling-induced increase in the charge transfer resistance has been attributed to side reaction products and to zinc dendrites [87].

In practical application scenario, the true areal capacity of the zinc anode plays vital role in enabling high energy ZABs. There are minimal reports in literature regarding stable zinc plating/striping behavior at an areal capacity equal to or above 5 mA h cm $^{-2}$ . With increasing amount of zinc being plated/stripped at every cycle, dendrites are expected to be a worse problem. As shown in Fig. S17 for bare ZF, as the plating capacity is increased from 2 mA h cm $^{-2}$  to 5 mA h cm $^{-2}$  there are more dendrites (consisting of zinc plate aggregates). Fig. 4(a) shows the surface morphology evolution of the LLP@ZF anode as a function of

electrodeposition capacity. This analysis was performed using symmetric cells. Plated samples are shown at 0 mA h cm<sup>-2</sup> (prior to deposition, pristine state), 5 mA h cm<sup>-2</sup>, 20 mA h cm<sup>-2</sup>, and 40 mA h cm<sup>-2</sup>. For the 5 mA h cm<sup>-2</sup> anode, the valleys are still discernable while the crests are flattened relative to the ridges that become widened. For the 20 mA h  ${\rm cm}^{-2}$  anode, the ridge areas are wide enough that the valleys appear as small divots in the surface. There is no evidence of preferential growth of the crests, such as would produce dendrites. As will be discussed with respect to the simulation results, this suppression of tip growth is due to the electrical field that is set up by the initial concaveconvex morphology. In the 40 mA h cm<sup>-2</sup> anode, the surface is flat with the initial concave-convex pattern being buried by the plated zinc. Fig. S18 shows the post-stripped 40 mA h cm<sup>-2</sup> LLP@ZF specimen, with all the plated zinc having been removed. Importantly, the figure demonstrates that the concave-convex pattern is largely recovered after the plated zinc was stripped. This stable geometry is expected to ensure long-term plating/stripping cyclability. The re-appearance of the concave-convex surface geometry is attributed to the plated zinc being stripped more easily than the underlying metal, in-turn due to the incorporation of some porosity and corrosion products in the deposit that enhance its dissolution kinetics.

Fig. 4(b)-(c) compare the cycling performance of symmetric cells

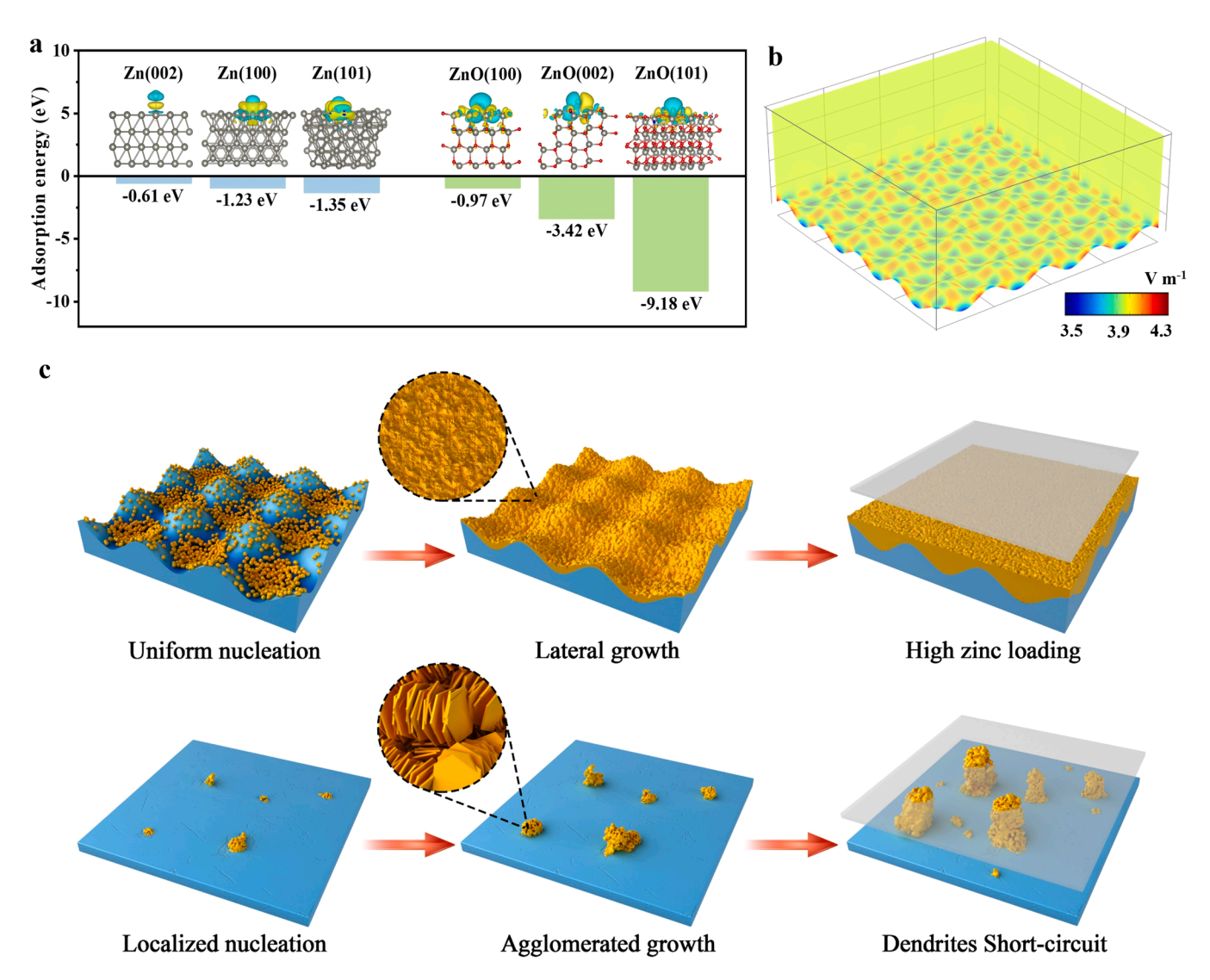


Fig. 5. (a) DFT calculated adsorption energies of Zn atoms on Zn and on ZnO crystal facets. Insets display the corresponding optimized atomic configurations of the adsorption complexes together with the differential charge density at the adsorption sites. (b) The simulation of electric field distributions at the vicinity of LLP@ZF surface. (c) Schematic illustration of the nucleation and growth behavior of (top) LLP@ZF versus (bottom) bare ZF.

based the three materials, at areal capacities of 20 mA h cm $^{-2}$  and 40 mA h cm $^{-2}$ , respectively. The bare ZF and ZnO@ZF based symmetric cells display sharp voltage drops at about 5 h, indicating cell short-circuits, in turn due to dendrite growth. The LLP@ZF cells can stably cycle for 520 h and 400 h, at which point the tests were concluded. For LLP@ZF the average overpotential was  $\sim 20$  mV, with minimal increase during the cycling regiment. Per Fig. 4(d) even at 50 mA h cm $^{-2}$ , the LLP@ZF based symmetric cell lasted for 400 h and displayed minimal overpotential increase. Fig. 4(e) highlights the performance of LLP@ZF anode as compared to the-state-of-the-art literature results. Included in the comparison are symmetric cell cycling performances with areal capacity above 2 mA h cm $^{-2}$  [38,41,61,78,84,88-99]. It may be observed that the LLP@ZF anode delivers the highest areal capacity (50 mA h cm $^{-2}$ ) and the longest lifespan (400 h).

Density Functional Theory (DFT) calculations were employed to understand the role of the surface oxide on the adsorption energy zinc ions. These results are shown in Fig. 5(a), with the detailed description of the DFT methodology being provided in the Supporting Information. Low-index (002), (100) and (101) crystal planes of hexagonal Zn and ZnO structures were employed for the zinc ion adsorption calculation. The adsorption energy is calculated as the energy of the surface with the Zn atom adsorbed minus sum the energy of the surface and of the Zn in isolation. To obtain the accurate adsorption energy, the most thermodynamically stable atomic configuration of the adsorption complex was established and employed in the calculation. The insets in Fig. 5(a) display the optimized atomic configuration of the adsorption complexes together with the differential charge density at the adsorption sites. The zinc atom adsorption energies on the low index ZnO planes are substantially higher than that on the low index Zn planes. For instance, the adsorption energies of Zn atom on ZnO (002) and (101) facets are respectively -3.42 and -9.18 eV, which are around 6 and 7 times the counterpart values for Zn facets. The adsorption energy for ZnO (100) is -0.97 eV, being somewhat less than the -1.23eV for Zn (100). These results indicate that in general, a ZnO surface is more zincophilic than a Zn surface, with strong preferential adsorption on the (101) and the (002) ZnO planes. A "philic" surface chemistry is known to promote dense nucleation and planar film growth during early-stage plating. Ongoing nucleation onto a continuous film, rather than onto discrete or agglomerated islands, has also been demonstrated to be a stability requisite during later stages of plating [100,101].

Finite element simulation was performed to understand the role of the concave-convex geometry on the electric field distribution at the vicinity of zinc anode surface. The details of the model construction are included in the Supporting Information. Fig. S19 displays the non-uniform electric field concentration around metal protrusions, such as those present on bare ZF anode surfaces. The electric field concentration at the tips is more than two times higher than at the flat surfaces (5.1 V m $^{-1}$  vs. 2.1 V m $^{-1}$ ), leading to enhanced Zn ion deposition rates in those regions. Once an island or a protrusion is formed on a planar Zn surface, such electric field concentrations are expected to drive dendritic growth, agreeing with earlier reports [102,103].

Fig. 5(b) displays a plot of the electric field fluctuation generated by the concave-convex pattern of LLP@ZF. All the ridge regions are red in color, indicating stronger electric field (4.3 V m<sup>-1</sup>) and hence more driving force for electrodeposition. The crests and the valley regions display lower electric field (3.5 V m<sup>-1</sup>) and hence less of a driving force. Based on this electric field distribution, the zinc electrodeposition rate at the ridge areas is faster than that at the crest and valley areas. As a result, the plated zinc will fill out the ridge areas first instead of piling up on the crest tips. Non-dendritic zinc electrodeposition would continue until a relatively flat electrode surface has formed, by which time the electric field becomes even. The simulation results agree well with the experimental observations. For example, per the 5 mAh cm<sup>-2</sup> capacity results shown in Fig. 4(a), the ridges are filled with no dendrites present.

The current density distribution in the vicinity of LLP@ZF and bare Zn surfaces was also simulated, per Fig. S20. The current density

distribution around a given surface geometry is consistent with the electric field fluctuation. Therefore, both types of simulations provide analogous insight into the source of dendrites in the system. It is worth noting that the fluctuation of the current density with LLP@ZF (ca. 0.4 mA cm<sup>-2</sup>) is much smaller than with bare ZF (ca. 1.6 mA cm<sup>-2</sup>). A more uniform current density across a metal surface is favorable for planar rather than dendritic electrodeposition/dissolution, agreeing with experimental results for LLP@ZF vs. bare Zn.

In-situ optical microscopy was employed to observe the dynamic process of zinc electrodeposition on LLP@ZF and bare ZF, the results being shown in Fig. S21. As shown in Fig. S21(a), the periodic concaveconvex geometry of LLP@ZF can be observed in the cross-sectional view. During the zinc plating at 10 mA cm<sup>-2</sup> the plated zinc fills the concave regions instead of piling up on the convex regions. With zinc plating capacity of 5 mAh cm<sup>-2</sup> (i.e. 30min), such concave regions were largely filled. By contrast, zinc deposition on bare ZF is highly nonuniform with isolated zinc clumps present on the surface. These observations agree well with the simulation findings. Fig. 5(c) contrasts the different electrodeposition behavior for LLP@ZF versus bare ZF, compiling the electrolyte wetting analysis, electrochemistry, microstructural characterization and multiscale simulation. It is experimentally demonstrated that the unique attributes of LLP@ZF include combined geometry and surface-chemistry induced hydrophilicity that allows for full wetting of the anode by the electrolyte. Density Functional Theory simulations reveal that LLP@ZF zincophilic surface chemistry is due a favorable energy of adsorption for zinc ions on the facets of the surface zinc oxide. Continuum simulations demonstrate that the concaveconvex patterned surface generates regular electrical field and associated current density fluctuations that suppresses tip-growth that otherwise is favored at pre-existing protrusions in planar foils. These attributes in sum ensure uniform zinc electrodeposition/electrostripping through a wide range of current densities, plated capacities and cycle numbers, without dendritic growth being triggered.

As proof-of-principle, we tested the viability of LLP@ZF in full aqueous zinc battery cells, with  $\alpha$ -MnO<sub>2</sub> based cathode in a 2 M ZnSO<sub>4</sub> + 0.1 M MnSO<sub>4</sub> solution. As a baseline, bare ZF was also tested as an anode in a full cell. Fig. S22 shows the nanowire morphology of the tetragonal  $\alpha\text{-MnO}_2$ . Fig. S23 shows the 5th cycle GCD profiles of bare ZF and LLP@ZF based full cells. At the current density of  $0.5 \text{ A g}^{-1}$ , the LLP@ZF cell exhibited the specific capacity of 256 mA h  $\rm g^{-1}$ , significantly higher than the 127 mA h  $g^{-1}$  with the bare ZF cell. It is notable that the voltage polarization of LLP@ZF||MnO2 cell (0.19 V) is lower than that of bare ZF||MnO<sub>2</sub> cell (0.27 V). Given the identical MnO<sub>2</sub> cathodes, the reduced voltage polarization is due to the more kinetically facile zinc plating/ striping. The CV curves in Fig. 6(a) further verify the improved kinetics in the full cell level. The LLP@ZF||MnO2 cell delivers a lower voltage for the anodic peak (by 46 mV) and a higher voltage for the cathodic peak (by 26/18 mV), as compared to those of bare ZF||MnO<sub>2</sub> cell. The higher currents of all characteristic peaks for the LLP@ZF||MnO2 cell indicate increased electrochemical activity and specific capacity, in line with the GCD results. Fig. 6(b) displays the rate performance of both cells at different current densities. As expected, the specific capacities of the LLP@ZF||MnO2 cell are higher than that of bare ZF||MnO2 cell at all rates, delivering average capacities of 243, 233, 202, 169 and 135 mA h  $\,$ g<sup>-1</sup> at currents of 0.2, 0.5, 1, 2 and 5 A g<sup>-1</sup>. A broad comparison with literature indicates that the rate performance of the LLP@ZF||MnO2 cell is among the most promising for state-of-the-art Zn||MnO2 batteries (Fig. S24 and Table S2) [31,34,38,61,84,85,89,104-109].

Fig. 6(c) shows the long term cyclability of the full cells. At the current density of 1 A g<sup>-1</sup>, the LLP@ZF||MnO<sub>2</sub> cell exhibits a reversible specific capacity of 173 mA h g<sup>-1</sup> after 500 cycles, leading to the capacity retention of 75 %. For the bare ZF||MnO<sub>2</sub> cell, the counterpart values are of 75 mA h g<sup>-1</sup> specific capacity and 39 % retention. The charge transfer resistance changes also reveal the discrepancy in the stability of the two full cells. As shown in Fig. S25, the uncycled full cells based on LLP@ZF and on bare Zn display  $R_{ct}$  values of 9.8  $\Omega$  and 115.0

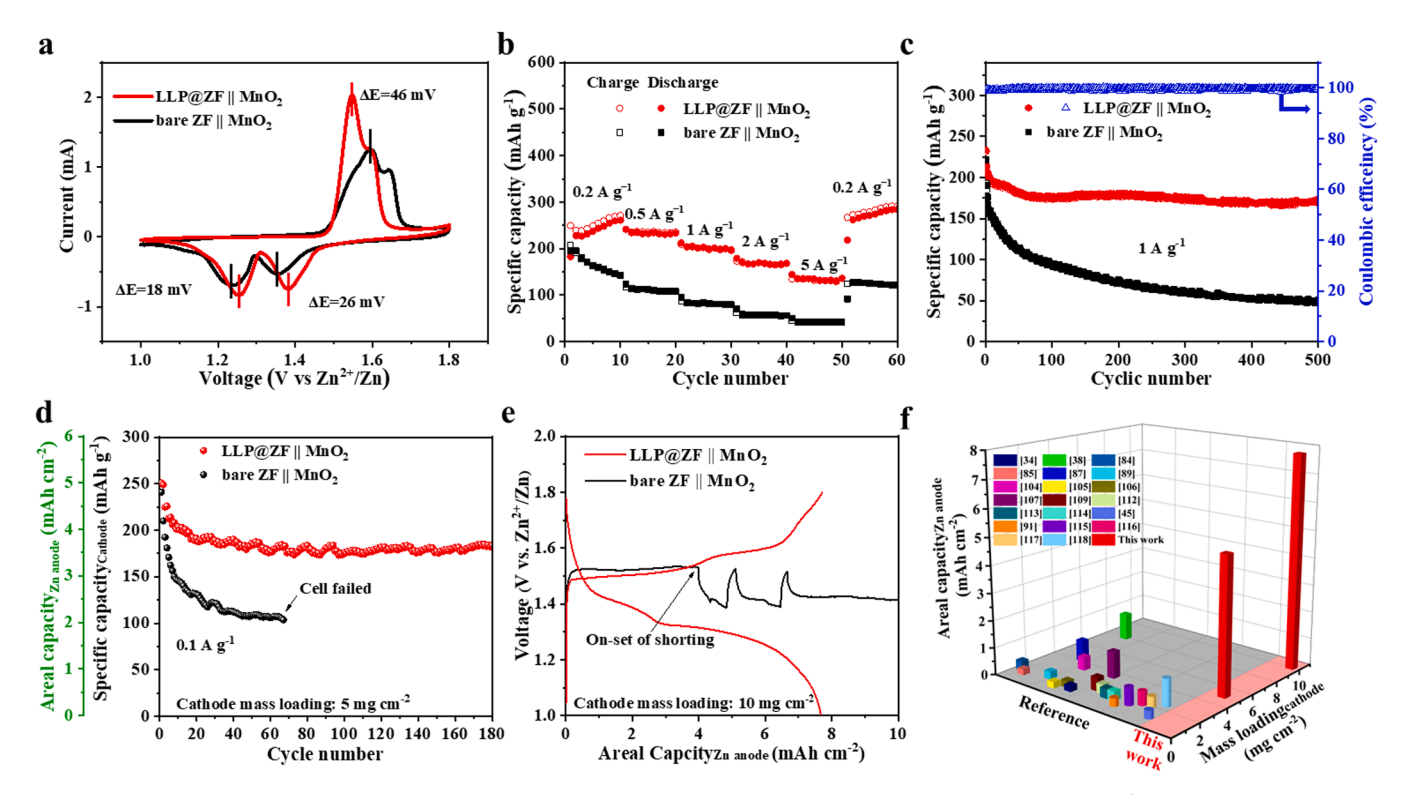


Fig. 6. Electrochemical performance of LLP@ZF||MnO<sub>2</sub> versus bare ZF||MnO<sub>2</sub> full cells, with cathode mass loading of 1-10 mg cm<sup>-2</sup>. (a) Cyclic voltammetry curves taken at 0.2 mV s<sup>-1</sup>; (b) Rate capability at different current densities; (c) Cycling performance at 1 A g<sup>-1</sup>. (d) Specific capacity and areal capacity versus cycle number, tested with a cathode mass loading of 5 mg cm<sup>-2</sup>. (e) Second cycle charging/discharging profiles of the two cells with cathode mass loading of 10 mg cm<sup>-2</sup>. (f) A comparison LLP@ZF||MnO<sub>2</sub> with state-of-the-art Zn ion full batteries from literature, with x-axis being cathode mass loading and y-axis being zinc anode areal capacity.

 $\Omega$ , respectively. After 500 cycles R<sub>ct</sub> increases to 15.2  $\Omega$  for LLP@ZF and to 402.2  $\Omega$  for bare Zn. In the first case the increase is by 50%, while in the second case the increase is by approximately 300%.

The mass loading of α-MnO<sub>2</sub> was increased to the commercial level of  $5-10 \text{ mg cm}^{-2}$  while utilizing  $0.25 \text{ cm}^{-2}$  size zinc anodes in the full cell. The areal capacities and the associated GCD profiles are displayed in Figs. 6(d) and S26, respectively. At MnO<sub>2</sub> loading of 5 mg cm<sup>-2</sup>, LLP@ZF cell delivered an initial areal capacity of 5.0 mA h cm<sup>-2</sup> normalized by the anode area. Per Fig. 6(d) reasonable capacity retention was achieved with the LLP@ZF||MnO2 with 0.15 % capacity decay per cycle and without electrical shorting. By contrast, the bare ZF cell displayed a much faster capacity decay rate, and electrical shorting failure at the 67<sup>th</sup> cycle. As demonstrated in Fig. 6(e), the bare ZF cell cannot survive for one complete cycle as the  $MnO_2$  loading is increased to 10 mg cm<sup>-2</sup>. Per the galvanostatic profile shown in Fig. 6(e), the bare ZF cell failed to finish the first charge due to an electrical short circuit, as evidenced by a sudden voltage drop in the profile. The short involves mixed ionelectron conduction in the internal circuit. At a certain point, however, the top of the zinc dendrite is striped and disconnected from the cathode. The cell then resumes charging, leading to the voltage increasing back up. The observed series of irregular voltage drops followed by voltage increases are due these short-circuit, mixed conducting self-discharge, and circuit opening steps. This mechanism is illustrated in Fig. S27 and is in agreement with refs [110,111].

The LLP@ZF cell worked well for prolonged tens of cycles with 10 mg cm $^{-2}$  MnO $_2$  loading and delivered maximum areal capacity of 7.6 mA h cm $^{-2}$ . Those results are illustrated in Fig. S28. Similar performance can also be obtained in the full cell employing a larger size anode (Fig. S29). Fig. 6(f) presents a side-by-side comparison of zinc areal capacities achieved in state-of-the-art aqueous zinc based full batteries from prior literature. This includes MnO $_2$  based cathodes [34,38,84,85,87,89,104-107,109,112-114] as well as VO $_x$  based cathodes [45,91,

115-118]. According to the figure, 7.6 mA h  $\rm cm^{-2}$  is the highest zinc anode areal capacity obtained in full cell configuration to date.

## 4. Conclusions

In summary, this study reports a state-of-the-art performance zincion battery (ZIB) based on a Laser Lithography Patterned Zinc Foils (LLP@ZF) from commercial zinc. In symmetric cells, LLP@ZF displays low plating/striping polarization and stable deep charge/discharge cycling. For example, LLP@ZF anode exhibits the initial nucleation overpotential as low as 3.8 mV at 1 mA cm<sup>-2</sup>, along with a cycling life of 400 h at areal capacity of 50 mA h cm<sup>-2</sup>. Exceptional full-cell performance is also achieved when LLP@ZF is coupled to a MnO<sub>2</sub> cathode with high mass loading of 10 mg cm<sup>-2</sup>, resulting in an unprecedented high areal capacity of 7.6 mA h cm<sup>-2</sup>. The periodically concave-convex LLP@ZF electrode is hydrophilic and zincophilic, leading to complete electrolyte wetting and uniform plating/stripping at various currents and capacities. Multiscale simulations reveal that the zinc oxide surface of LLP@ZF provides a more negative energy of adsorption for zinc ions versus the baseline metallic zinc, while its concave-convex geometry provides favorable electrical field distribution to suppress dendrite growth.

# CRediT authorship contribution statement

Zechuan Huang: Conceptualization, Data curation, Formal analysis, Investigation, Methodology, Software, Visualization, Writing – original draft. Haoyang Li: Resources, Formal analysis, Writing – original draft. Zhen Yang: Resources, Validation, Writing – review & editing. Haozhi Wang: Software, Data curation, Writing – original draft. Jingnan Ding: Visualization, Writing – original draft. Luyao Xu: Software, Data curation, Writing – original draft. Yanling Tian: Resources, Methodology.

David Mitlin: Formal analysis, Methodology, Funding acquisition, Supervision, Validation, Writing – review & editing. Jia Ding: Conceptualization, Methodology, Funding acquisition, Investigation, Methodology, Project administration, Supervision, Validation, Writing – review & editing. Wenbin Hu: Project administration, Supervision, Validation, Writing – review & editing.

#### **Declaration of Competing Interest**

The authors declare that they have no known competing financial interests or personal relationships that could have appeared to influence the work reported in this paper.

## Acknowledgements

J.D. (conceive idea, manuscript preparation, supervision) were funded by the financial support from the National Natural Science Foundation of China (No. 52072257) and the support from the National Key Research and Development Program of China (No.:2019YFE0118800). D.M. (research co-conception and guidance, manuscript preparation) is supported by the National Science Foundation, CMMI, Div. Of Civil. Mechanical, & Manufact. Inn., Award Number 1911905.

#### Supplementary materials

Supplementary material associated with this article can be found, in the online version, at doi:10.1016/j.ensm.2022.06.054.

#### References

- M.S. Dresselhaus, I.L. Thomas, Alternative energy technologies, Nature 414 (2001) 332–337.
- [2] B. Dunn, H. Kamath, J.-M. Tarascon, Electrical energy storage for the grid: a battery of choices, Science 334 (2011) 928–935.
- [3] W. Gao, S. Liang, R. Wang, Q. Jiang, Y. Zhang, Q. Zheng, B. Xie, C.Y. Toe, X. Zhu, J. Wang, Industrial carbon dioxide capture and utilization: state of the art and future challenges, Chem. Soc. Rev. 49 (2020) 8584–8686.
- [4] S. Fleischmann, J.B. Mitchell, R. Wang, C. Zhan, D.-e. Jiang, V. Presser, V. Augustyn, Pseudocapacitance: from fundamental understanding to high power energy storage materials, Chem. Rev. 120 (2020) 6738–6782.
- [5] Q. Dou, H.S. Park, Perspective on high-energy carbon-based supercapacitors, Energy Environ. Mater. 3 (2020) 286–305.
- [6] A.S. Lakhnot, T. Gupta, Y. Singh, P. Hundekar, R. Jain, F. Han, N. Koratkar, Aqueous lithium-ion batteries with niobium tungsten oxide anodes for superior volumetric and rate capability, Energy Storage Mater 27 (2020) 506–513.
- [7] R. Zhu, H. Duan, Z. Zhao, H. Pang, Recent progress of dimensionally designed electrode nanomaterials in aqueous electrochemical energy storage, J. Mater. Chem. A 9 (2021) 9535–9572.
- [8] J. Ding, Y. Wang, Z. Huang, W. Song, C. Zhong, J. Ding, W. Hu, Toward theoretical capacity and superhigh power density for potassium-selenium batteries via facilitating reversible potassiation kinetics, ACS Appl. Mater. Interfaces 14 (2022) 6828–6840.
- [9] J. Lin, J. Ding, H. Wang, X. Yang, X. Zheng, Z. Huang, W. Song, J. Ding, X. Han, W. Hu, Boosting energy efficiency and stability of Li–CO2 batteries via synergy between Ru atom clusters and single-atom Ru–N4 sites in the electrocatalyst cathode, Adv. Mater. (2022), 2200559.
- [10] C. Xiao, W. Song, J. Liang, J. Zhang, Z. Huang, J. Zhang, H. Wang, C. Zhong, J. Ding, W. Hu, P-block tin single atom catalyst for improved electrochemistry in lithium-sulfur battery: a theoretical and experimental study, J. Mater. Chem. A (2022).
- [11] M.J. Wu, G.X. Zhang, M.H. Wu, J. Prakash, S.H. Sun, Rational design of multifunctional air electrodes for rechargeable Zn-Air batteries: recent progress and future perspectives, Energy Storage Mater. 21 (2019) 253–286.
- [12] M.B. Lim, T.N. Lambert, B.R. Chalamala, Rechargeable alkaline zinc-manganese oxide batteries for grid storage: mechanisms, challenges and developments, Mater. Sci. Eng. R-Rep. 143 (2021) 24.
- [13] W. Zhou, D. Zhu, J. He, J. Li, H. Chen, Y. Chen, D. Chao, A scalable top-down strategy toward practical metrics of Ni–Zn aqueous batteries with total energy densities of 165 W h kg- 1 and 506 W h L- 1, Energy Environ. Sci. 13 (2020) 4157–4167.
- [14] Y.W. Zhao, D.H. Wang, X.L. Li, Q. Yang, Y. Guo, F.N. Mo, Q. Li, C.X. Peng, H.F. Li, C.Y. Zhi, Initiating a reversible aqueous Zn/sulfur battery through a "Liquid Film", Adv. Mater. 32 (2020) 10.
- [15] C. Han, W. Li, H.K. Liu, S. Dou, J. Wang, Principals and strategies for constructing a highly reversible zinc metal anode in aqueous batteries, Nano Energy 74 (2020), 104523.

- [16] W. Fan, J. Ding, J. Ding, Y. Zheng, W. Song, J. Lin, C. Xiao, C. Zhong, H. Wang, W. Hu, Identifying heteroatomic and defective sites in carbon with dual-ion adsorption capability for high energy and power zinc ion capacitor, Nano-Micro Lett. 13 (2021) 1–18.
- [17] C. Li, X. Xie, S. Liang, J. Zhou, Issues and future perspective on zinc metal anode for rechargeable aqueous zinc-ion batteries, Energy Environ. Mater. 3 (2020) 146–159.
- [18] T.M. Gür, Review of electrical energy storage technologies, materials and systems: challenges and prospects for large-scale grid storage, Energy Environ. Sci. 11 (2018) 2696–2767.
- [19] B. Tang, L. Shan, S. Liang, J. Zhou, Issues and opportunities facing aqueous zincion batteries, Energy Environ. Sci. 12 (2019) 3288–3304.
- [20] H. Jia, Z. Wang, B. Tawiah, Y. Wang, C.-Y. Chan, B. Fei, F. Pan, Recent advances in zinc anodes for high-performance aqueous Zn-ion batteries, Nano Energy 70 (2020), 104523.
- [21] J. Hao, X. Li, X. Zeng, D. Li, J. Mao, Z. Guo, Deeply understanding the Zn anode behaviour and corresponding improvement strategies in different aqueous Znbased batteries, Energy Environ. Sci. 13 (2020) 3917–3949.
- [22] L. Yuan, J. Hao, C.-C. Kao, C. Wu, H.-K. Liu, S.-X. Dou, S.-Z. Qiao, Regulation methods for the Zn/electrolyte interphase and the effectiveness evaluation in aqueous Zn-ion batteries, Energy Environ. Sci. 14 (2021) 5669–5689.
- [23] Z. Cao, P. Zhuang, X. Zhang, M. Ye, J. Shen, P.M. Ajayan, Strategies for dendrite-free anode in aqueous rechargeable zinc ion batteries, Adv. Energy Mater. 10 (2020), 2001599.
- [24] L. Ma, M.A. Schroeder, O. Borodin, T.P. Pollard, M.S. Ding, C. Wang, K. Xu, Realizing high zinc reversibility in rechargeable batteries, Cah. Inf. Tech./Rev Metall. 5 (2020) 743–749.
- [25] L. Cao, D. Li, T. Deng, Q. Li, C. Wang, Hydrophobic organic-electrolyte-protected zinc anodes for aqueous zinc batteries, Angew. Chem. Int. Ed. 59 (2020) 19292–19296.
- [26] Z. Wang, J. Huang, Z. Guo, X. Dong, Y. Liu, Y. Wang, Y. Xia, A metal-organic framework host for highly reversible dendrite-free zinc metal anodes, Joule 3 (2019) 1289–1300.
- [27] A. Naveed, H. Yang, Y. Shao, J. Yang, N. Yanna, J. Liu, S. Shi, L. Zhang, A. Ye, B. He, J. Wang, A highly reversible zn anode with intrinsically safe organic electrolyte for long-cycle-life batteries. Adv. Mater. 31 (2019), 1900668.
- [28] K. Wang, P. Pei, Z. Ma, H. Chen, H. Xu, D. Chen, X. Wang, Dendrite growth in the recharging process of zinc-air batteries, J. Mater. Chem. A 3 (2015) 22648–22655.
- [29] Q. Yang, G.J. Bang, Y. Guo, Z.X. Liu, B.X. Yon, D.H. Wang, Z.D. Huang, X.L. Li, J. Fan, C.Y. Zhi, Do zinc dendrites exist in neutral zinc batteries: a developed electrohealing strategy to in situ rescue in-service batteries, Adv. Mater. 31 (2019) 9.
- [30] P. Liu, Z. Zhang, R. Hao, Y. Huang, W. Liu, Y. Tan, P. Li, J. Yan, K. Liu, Ultra-highly stable zinc metal anode via 3D-printed g-C3N4 modulating interface for long life energy storage systems, Chem. Eng. J. 403 (2021).
- [31] X. Zhou, P. Cao, A. Wei, A. Zou, H. Ye, W. Liu, J. Tang, J. Yang, Driving the interfacial ion-transfer kinetics by mesoporous TiO2 spheres for highperformance aqueous Zn-Ion batteries, ACS Appl. Mater. Interfaces 13 (2021) 8181–8190.
- [32] Q. Yang, Y. Guo, B. Yan, C. Wang, Z. Liu, Z. Huang, Y. Wang, Y. Li, H. Li, L. Song, Hydrogen-substituted graphdiyne ion tunnels directing concentration redistribution for commercial-grade dendrite-free zinc anodes, Adv. Mater. 32 (2020), 2001755.
- [33] L. Kang, M. Cui, F. Jiang, Y. Gao, H. Luo, J. Liu, W. Liang, C. Zhi, Nanoporous CaCO3 coatings enabled uniform zn stripping/plating for long-life zinc rechargeable aqueous batteries, Adv. Energy Mater. 8 (2018), 1801090.
- [34] A. Bayaguud, X. Luo, Y. Fu, C. Zhu, Cationic surfactant-type electrolyte additive enables three-dimensional dendrite-free zinc anode for stable zinc-ion batteries, ACS Energy Lett. 5 (2020) 3012–3020.
- [35] K.E. Sun, T.K. Hoang, T.N.L. Doan, Y. Yu, X. Zhu, Y. Tian, P. Chen, Suppression of dendrite formation and corrosion on zinc anode of secondary aqueous batteries, ACS Appl. Mater. Interfaces 9 (2017) 9681–9687.
- [36] J. Cao, D. Zhang, X. Zhang, M. Sawangphruk, J. Qin, R. Liu, A universal and facile approach to suppress dendrite formation for a Zn and Li metal anode, J. Mater. Chem. A 8 (2020) 9331–9344.
- [37] L. Dong, W. Yang, W. Yang, H. Tian, Y. Huang, X. Wang, C. Xu, C. Wang, F. Kang, G. Wang, Flexible and conductive scaffold-stabilized zinc metal anodes for ultralong-life zinc-ion batteries and zinc-ion hybrid capacitors, Chem. Eng. J. 384 (2020), 123355.
- [38] R. Yuksel, O. Buyukcakir, W.K. Seong, R.S. Ruoff, Metal-organic framework integrated anodes for aqueous zinc-ion batteries, Adv. Energy Mater. 10 (2020), 1904215.
- [39] B. Bozzini, C. Mele, A. Veneziano, N. Sodini, G. Lanzafame, A. Taurino, L. Mancini, Morphological evolution of Zn-sponge electrodes monitored by in situ X-ray computed microtomography, ACS Appl. Mater. Interfaces 3 (2020) 4931–4940.
- [40] X. Shi, G. Xu, S. Liang, C. Li, S. Guo, X. Xie, X. Ma, J. Zhou, Homogeneous deposition of zinc on three-dimensional porous copper foam as a superior zinc metal anode, ACS Sustain. Chem. Eng. 7 (2019) 17737–17746.
- [41] Y. Zeng, X. Zhang, R. Qin, X. Liu, P. Fang, D. Zheng, Y. Tong, X. Lu, Dendrite-free zinc deposition induced by multifunctional CNT frameworks for stable flexible Zn-ion batteries, Adv. Mater. 31 (2019), 1903675.
- [42] Y. Tian, Y. An, C. Wei, B. Xi, S. Xiong, J. Feng, Y. Qian, Flexible and free-standing Ti3C2Tx MXene@Zn paper for dendrite-free aqueous zinc metal batteries and nonaqueous lithium metal batteries, ACS Nano 13 (2019) 11676–11685.

- [43] H. Liu, G. Zhang, L. Wang, X. Zhang, Z. Zhao, F. Chen, L. Song, H. Duan, Engineering 3D architecture electrodes for high-rate aqueous Zn–Mn microbatteries, ACS Appl. Energy Mater. 4 (2021) 10414–10422.
- [44] H. Liu, J. Li, X. Zhang, X. Liu, Y. Yan, F. Chen, G. Zhang, H. Duan, Ultrathin and ultralight Zn micromesh-induced spatial-selection deposition for flexible highspecific-energy Zn-Ion batteries, Adv. Funct. Mater. 31 (2021), 2106550.
- [45] G. Zhang, X. Zhang, H. Liu, J. Li, Y. Chen, H. Duan, 3D-printed multi-channel metal lattices enabling localized electric-field redistribution for dendrite-free aqueous Zn Ion batteries, Adv. Energy Mater. 11 (2021), 2003927.
- [46] M. Malinauskas, A. Žukauskas, S. Hasegawa, Y. Hayasaki, V. Mizeikis, R. Buividas, S. Juodkazis, Ultrafast laser processing of materials: from science to industry, Light. Sci. Appl. 5 (2016) e16133-e16133.
- [47] S. Lei, X. Zhao, X. Yu, A. Hu, S. Vukelic, M.B. Jun, H.-E. Joe, Y.L. Yao, Y.C. Shin, Ultrafast laser applications in manufacturing processes: a state-of-the-art review, J. Manuf. Sci. Eng. 142 (2020), 031005.
- [48] R. Stoian, J.-P. Colombier, Advances in ultrafast laser structuring of materials at the nanoscale, Nanophotonics 9 (2020) 4665–4688.
- [49] B. Wu, G. Zhang, M. Yan, T. Xiong, P. He, L. He, X. Xu, L. Mai, Graphene scroll-coated α-MnO2 nanowires as high-performance cathode materials for aqueous Zn-ion battery, Small 14 (2018), 1703850.
- [50] J. Li, H. Zhao, M. Wang, Y. Zhu, B. Li, X. Yu, J. Xu, Y. Cheng, L. Ouyang, H. Shao, Rational design of 3D N-doped carbon nanosheet framework encapsulated ultrafine ZnO nanocrystals as superior performance anode materials in lithium ion batteries, J. Mater. Chem. A 7 (2019) 25155–25164.
- [51] F.C. Porter, Corrosion Resistance of Zinc and Zinc Alloys, CRC Press, 1994.
- [52] D.R. Lide, CRC Handbook of Chemistry and Physics, CRC press, 2006.
- [53] E.P. DeGarmo, J.T. Black, R.A. Kohser, B.E. Klamecki, Materials and Process in Manufacturing, Prentice Hall, Upper Saddle River, 1997.
- [54] Z. Zhao, J. Zhao, Z. Hu, J. Li, J. Li, Y. Zhang, C. Wang, G. Cui, Long-life and deeply rechargeable aqueous Zn anodes enabled by a multifunctional brightenerinspired interphase, Energy Environ. Sci. 12 (2019) 1938–1949.
- [55] H. Tian, Z. Li, G. Feng, Z. Yang, D. Fox, M. Wang, H. Zhou, L. Zhai, A. Kushima, Y. Du, Z. Feng, X. Shan, Y. Yang, Stable, high-performance, dendrite-free, seawater-based aqueous batteries, Nat. Commun. 12 (2021) 237.
- [56] F. Dabby, U.-C. Paek, High-intensity laser-induced vaporization and explosion of solid material, IEEE J. Quantum Electron. 8 (1972) 106–111.
- [57] M. Aden, E. Beyer, G. Herziger, H. Kunze, Laser-induced vaporization of a metal surface, J. Phys. D 25 (1992) 57.
- [58] N. Bulgakova, A. Bulgakov, Pulsed laser ablation of solids: transition from normal vaporization to phase explosion, Appl. Phys. A 73 (2001) 199–208.
- [59] J. Jia, M. Li, C.V. Thompson, Amorphization of silicon by femtosecond laser pulses, Appl. Phys. Lett. 84 (2004) 3205–3207.
- [60] J. Sun, S.K. Sinha, A. Khammari, M. Picher, M. Terrones, F. Banhart, The amorphization of metal nanoparticles in graphitic shells under laser pulses, Carbon 161 (2020) 495–501.
- [61] Q. Zhang, J. Luan, X. Huang, Q. Wang, D. Sun, Y. Tang, X. Ji, H. Wang, Revealing the role of crystal orientation of protective layers for stable zinc anode, Nat. Commun. 11 (2020) 1–7.
- [62] Q. Zhang, J. Luan, Y. Tang, X. Ji, S. Wang, H. Wang, A facile annealing strategy for achieving in situ controllable Cu 2 O nanoparticle decorated copper foil as a current collector for stable lithium metal anodes, J. Mater. Chem. A 6 (2018) 18444–18448.
- [63] S. Zhang, J. Huang, Z. Chen, S. Yang, Y. Lai, Liquid mobility on superwettable surfaces for applications in energy and the environment, J. Mater. Chem. A 7 (2019) 38–63.
- [64] B. Su, Y. Tian, L. Jiang, Bioinspired interfaces with superwettability: from materials to chemistry, J. Am. Chem. Soc. 138 (2016) 1727–1748.
- [65] Y. Liang, H. Dong, D. Aurbach, Y. Yao, Current status and future directions of multivalent metal-ion batteries, Nat. Energy 5 (2020) 646–656.
- [66] Q. Yang, Q. Li, Z. Liu, D. Wang, Y. Guo, X. Li, Y. Tang, H. Li, B. Dong, C. Zhi, Dendrites in Zn-based batteries, Adv. Mater. 32 (2020), 2001854.
- [67] Y. Zhang, G. Yang, M.L. Lehmann, C. Wu, L. Zhao, T. Saito, Y. Liang, J. Nanda, Y. Yao, Separator effect on zinc electrodeposition behavior and its implication for zinc battery lifetime, Nano Lett. 21 (2021) 10446–10452.
- [68] Q. Zhang, J. Luan, Y. Tang, X. Ji, H. Wang, Interfacial design of dendrite-free zinc anodes for aqueous zinc-ion batteries, Angew. Chem. Int. Ed. 59 (2020) 13180–13191.
- [69] Y. Guo, R. Wang, C. Cui, R. Xiong, Y. Wei, T. Zhai, H. Li, Shaping Li deposits from wild dendrites to regular crystals via the ferroelectric effect, Nano Lett. 20 (2020) 7680–7687
- [70] P. Liu, H. Hao, H. Celio, J. Cui, M. Ren, Y. Wang, H. Dong, A.R. Chowdhury, T. Hutter, F.A. Perras, Multifunctional separator allows stable cycling of potassium metal anodes and of potassium metal batteries, Adv. Mater. (2021), 2105855.
- [71] F. Xie, H. Li, X. Wang, X. Zhi, D. Chao, K. Davey, S.-Z. Qiao, Mechanism for zincophilic sites on zinc-metal anode hosts in aqueous batteries, Adv. Energy Mater. 11 (2021), 2003419.
- [72] P. Liang, J. Yi, X. Liu, K. Wu, Z. Wang, J. Cui, Y. Liu, Y. Wang, Y. Xia, J. Zhang, Highly reversible Zn anode enabled by controllable formation of nucleation sites for Zn-based batteries, Adv. Funct. Mater. 30 (2020), 1908528.
- [73] Q. Yang, Y. Guo, B. Yan, C. Wang, Z. Liu, Z. Huang, Y. Wang, Y. Li, H. Li, L. Song, Hydrogen-substituted graphdiyne ion tunnels directing concentration redistribution for commercial-grade dendrite-free zinc anodes, Adv. Mater. (2020), 2001755.

- [74] J. Zhao, J. Zhang, W. Yang, B. Chen, Z. Zhao, H. Qiu, S. Dong, X. Zhou, G. Cui, L. Chen, Water-in-deep eutectic solvent" electrolytes enable zinc metal anodes for rechargeable aqueous batteries, Nano Energy 57 (2019) 625–634.
- [75] Y. Cui, Q. Zhao, X. Wu, X. Chen, J. Yang, Y. Wang, R. Qin, S. Ding, Y. Song, J. Wu, K. Yang, Z. Wang, Z. Mei, Z. Song, H. Wu, Z. Jiang, G. Qian, L. Yang, F. Pan, An interface-bridged organic-inorganic layer that suppresses dendrite formation and side reactions for ultra-long-life aqueous zinc metal anodes, Angew. Chem. Int. Ed. 59 (2020) 16594–16601.
- [76] L. Ma, Q. Li, Y. Ying, F. Ma, S. Chen, Y. Li, H. Huang, C. Zhi, Toward practical high-areal-capacity aqueous zinc-metal batteries: quantifying hydrogen evolution and a solid-ion conductor for stable zinc anodes, Adv. Mater. 33 (2021), 2007406.
- [77] M. Zhou, S. Guo, J. Li, X. Luo, Z. Liu, T. Zhang, X. Cao, M. Long, B. Lu, A. Pan, G. Fang, J. Zhou, S. Liang, Surface-preferred crystal plane for a stable and reversible zinc anode, Adv. Mater. 33 (2021), 2100187.
- [78] C. Li, Z. Sun, T. Yang, L. Yu, N. Wei, Z. Tian, J. Cai, J. Lv, Y. Shao, M.H. Rummeli, J. Sun, Z. Liu, Directly grown vertical graphene carpets as janus separators toward stabilized Zn metal anodes, Adv. Mater. 32 (2020), 2003425.
- [79] D. Yuan, J. Zhao, H. Ren, Y. Chen, R. Chua, E.T.J. Jie, Y. Cai, E. Edison, W. Manalastas Jr., M.W. Wong, M. Srinivasan, Anion texturing towards dendritefree Zn anode for aqueous rechargeable batteries, Angew. Chem. Int. Ed. 133 (2021) 7289–7295.
- [80] P. Zou, R. Zhang, L. Yao, J. Qin, K. Kisslinger, H. Zhuang, H.L. Xin, Ultrahigh-rate and long-life zinc-metal anodes enabled by self-accelerated cation migration, Adv. Energy Mater. 11 (2021), 2100982.
- [81] V. Yufit, F. Tariq, D.S. Eastwood, M. Biton, B. Wu, P.D. Lee, N.P. Brandon, Operando visualization and multi-scale tomography studies of dendrite formation and dissolution in zinc batteries, Joule 3 (2019) 485–502.
- [82] M. Biton, F. Tariq, V. Yufit, Z. Chen, N. Brandon, Integrating multi-length scale high resolution 3D imaging and modelling in the characterisation and identification of mechanical failure sites in electrochemical dendrites, Acta Mater. 141 (2017) 39–46.
- [83] D. Han, S. Wu, S. Zhang, Y. Deng, C. Cui, L. Zhang, Y. Long, H. Li, Y. Tao, Z. Weng, Q.-H. Yang, F. Kang, A corrosion-resistant and dendrite-free zinc metal anode in aqueous systems, Small 16 (2020), 20010736.
- [84] R. Zhao, Y. Yang, G. Liu, R. Zhu, J. Huang, Z. Chen, Z. Gao, X. Chen, L. Qie, Redirected Zn electrodeposition by an anti-corrosion elastic constraint for highly reversible Zn anodes, Adv. Funct. Mater. 31 (2020), 2001867.
- [85] Y. Yang, C. Liu, Z. Lv, H. Yang, Y. Zhang, M. Ye, L. Chen, J. Zhao, C.C. Li, Synergistic manipulation of Zn2+ ion flux and desolvation effect enabled by anodic growth of a 3D ZnF2 matrix for long-lifespan and dendrite-free Zn metal anodes. Adv. Mater. 33 (2021), 2007388.
- [86] H. He, H. Tong, X. Song, X. Song, J. Liu, Highly stable Zn metal anodes enabled by atomic layer deposited Al2O3 coating for aqueous zinc-ion batteries, J. Mater. Chem. A 8 (2020) 7836–7846.
- [87] X. Zhang, J. Li, D. Liu, M. Liu, T. Zhou, K. Qi, L. Shi, Y. Zhu, Y. Qian, Ultra-long-life and highly reversible Zn metal anodes enabled by a desolvation and deanionization interface layer dagger, Energy Environ. Sci. 14 (2021) 3120–3129.
- [88] H. Yang, Y. Qiao, Z. Chang, H. Deng, P. He, H. Zhou, A metal-organic framework as a multifunctional ionic sieve membrane for long-life aqueous zinc-iodide batteries, Adv. Mater. 32 (2020), 2004240.
- [89] J.Y. Kim, G. Liu, G.Y. Shim, H. Kim, J.K. Lee, Functionalized Zn@ZnO hexagonal pyramid array for dendrite-free and ultrastable zinc metal anodes, Adv. Funct. Mater. 30 (2020), 2004210.
- [90] W. Guo, Z. Cong, Z. Guo, C. Chang, X. Liang, Y. Liu, W. Hu, X. Pu, Dendrite-free Zn anode with dual channel 3D porous frameworks for rechargeable Zn batteries, Energy Storage Mater. 30 (2020) 104–112.
- [91] Q. Lu, C. Liu, Y. Du, X. Wang, L. Ding, A. Omar, D. Mikhailova, Uniform Zn deposition achieved by Ag coating for improved aqueous zinc-ion batteries, ACS Appl. Mater. Interfaces 13 (2021) 16869–16875.
- [92] Q. Zhang, J. Luan, L. Fu, S. Wu, Y. Tang, X. Ji, H. Wang, The three-dimensional dendrite-free zinc anode on a copper mesh with a zinc-oriented polyacrylamide electrolyte additive, Angew. Chem. Int. Ed. 58 (2019) 15841–15847.
- [93] H. Lu, X. Zhang, M. Luo, K. Cao, Y. Lu, B.B. Xu, H. Pan, K. Tao, Y. Jiang, Amino acid-induced interface charge engineering enables highly reversible Zn anode, Adv. Funct. Mater. 31 (2021), 2103514.
- [94] J. Zhou, M. Xie, F. Wu, Y. Mei, Y. Hao, R. Huang, G. Wei, A. Liu, L. Li, R. Chen, Ultrathin surface coating of nitrogen-doped graphene enables stable zinc anodes for aqueous zinc-ion batteries, Adv. Mater. 33 (2021), 2101649.
- [95] W. Zhou, M. Chen, Q. Tian, J. Chen, X. Xu, C.-P. Wong, Cotton-derived cellulose film as a dendrite-inhibiting separator to stabilize the zinc metal anode of aqueous zinc ion batteries, Energy Storage Mater. 44 (2022) 57–65.
- [96] W. Du, S. Huang, Y. Zhang, M. Ye, C.C. Li, Enable commercial Zinc powders for dendrite-free Zinc anode with improved utilization rate by pristine graphene hybridization, Energy Storage Mater. 45 (2022) 465–473.
- [97] W. Yuan, G. Ma, X. Nie, Y. Wang, S. Di, L. Wang, J. Wang, S. Shen, N. Zhang, Insitu construction of a hydroxide-based solid electrolyte interphase for robust zinc anodes, Chem. Eng. J. 431 (2022), 134076.
- [98] Z. Guo, L. Fan, C. Zhao, A. Chen, N. Liu, Y. Zhang, N. Zhang, A dynamic and self-adapting interface coating for stable Zn-metal anodes, Adv. Mater. 34 (2022), 210(12)
- [99] S. Xie, Y. Li, X. Li, Y. Zhou, Z. Dang, J. Rong, L. Dong, Stable zinc anodes enabled by zincophilic Cu nanowire networks, Nano-Micro Lett. 14 (2022) 1–13.
- [100] P. Liu, Y. Wang, Q. Gu, J. Nanda, J. Watt, D. Mitlin, Dendrite-free potassium metal anodes in a carbonate electrolyte, Adv. Mater. 32 (2020), 1906735.

- [101] T. Foroozan, V. Yurkiv, S. Sharifi-Asl, R. Rojaee, F. Mashayek, R. Shahbazian-Yassar, Non-dendritic Zn electrodeposition enabled by zincophilic graphene substrates, ACS Appl. Mater. Interfaces 11 (2019) 44077–44089.
- [102] M. Liu, L. Yang, H. Liu, A. Amine, Q. Zhao, Y. Song, J. Yang, K. Wang, F. Pan, Artificial solid-electrolyte interface facilitating dendrite-free zinc metal anodes via nanowetting effect, ACS Appl. Mater. Interfaces 11 (2019) 32046–32051.
- [103] M. Cui, Y. Xiao, L. Kang, W. Du, Y. Gao, X. Sun, Y. Zhou, X. Li, H. Li, F. Jiang, C. Zhi, Quasi-isolated Au particles as heterogeneous seeds to guide uniform Zn deposition for aqueous zinc-ion batteries, ACS Appl. Energy Mater. 2 (2019) 6490–6496.
- [104] W. Xu, K. Zhao, W. Huo, Y. Wang, G. Yao, X. Gu, H. Cheng, L. Mai, C. Hu, X. Wang, Diethyl ether as self-healing electrolyte additive enabled long-life rechargeable aqueous zinc ion batteries, Nano Energy 62 (2019) 275–281.
- [105] S. Chen, R. Lan, J. Humphreys, S. Tao, Salt-concentrated acetate electrolytes for a high voltage aqueous Zn/MnO2 battery, Energy Storage Mater. 28 (2020) 205–215
- [106] J. Hao, B. Li, X. Li, X. Zeng, S. Zhang, F. Yang, S. Liu, D. Li, C. Wu, Z. Guo, An indepth study of Zn metal surface chemistry for advanced aqueous Zn-Ion batteries, Adv. Mater. 32 (2020), 2003021.
- [107] M. Liu, J. Cai, H. Ao, Z. Hou, Y. Zhu, Y. Qian, NaTi2(PO4)(3)solid-state electrolyte protection layer on Zn metal anode for superior long-life aqueous zinc-ion batteries, Adv. Funct. Mater. 30 (2020), 2004855.
- [108] C. Wu, H. Tan, W. Huang, W. Li, D. Khang Ngoc, C. Yan, W. Wei, L. Chen, Q. Yan, A new scalable preparation of metal nanosheets: potential applications for aqueous Zn-Ion batteries anode, Adv. Funct. Mater. 30 (2020), 2003187.
- [109] H. Yang, Z. Chang, Y. Qiao, H. Deng, X. Mu, P. He, H. Zhou, Constructing a supersaturated electrolyte front surface for stable rechargeable aqueous zinc batteries, Angew. Chem. Int. Ed. 59 (2020) 9377–9381.

- [110] M.S. Gonzalez, Q. Yan, J. Holoubek, Z. Wu, H. Zhou, N. Patterson, V. Petrova, H. Liu, P. Liu, Draining over blocking: nano-composite janus separators for mitigating internal shorting of lithium batteries, Adv. Mater. 32 (2020), 1906836.
- [111] B. Liu, Y. Jia, J. Li, S. Yin, C. Yuan, Z. Hu, L. Wang, Y. Li, J. Xu, Safety issues caused by internal short circuits in lithium-ion batteries, J. Mater. Chem. A 6 (2018) 21475–21484.
- [112] Y. Wang, Y. Chen, W. Liu, X. Ni, P. Qing, Q. Zhao, W. Wei, X. Ji, J. Ma, L. Chen, Uniform and dendrite-free zinc deposition enabled by in situ formed AgZn3 for the zinc metal anode, J. Mater. Chem. A 9 (2021) 8452–8461.
- [113] Z. Wang, L. Dong, W. Huang, H. Jia, Q. Zhao, Y. Wang, B. Fei, F. Pan, Simultaneously regulating uniform Zn2+ flux and electron conduction by MOF/ rGO interlayers for high-performance Zn anodes, Nano-Micro Lett. 13 (2021) 1-11
- [114] Y. Zhang, G. Wang, F. Yu, G. Xu, Z. Li, M. Zhu, Z. Yue, M. Wu, H.-K. Liu, S.-X. Dou, C. Wu, Highly reversible and dendrite-free Zn electrodeposition enabled by a thin metallic interfacial layer in aqueous batteries, Chem. Eng. J. 416 (2021), 128062.
- [115] J. Cong, X. Shen, Z. Wen, X. Wang, L. Peng, J. Zeng, J. Zhao, Ultra-stable and highly reversible aqueous zinc metal anodes with high preferred orientation deposition achieved by a polyanionic hydrogel electrolyte, Energy Storage Mater. 35 (2021) 586–594.
- [116] X. Liu, F. Yang, W. Xu, Y. Zeng, J. He, X. Lu, Zeolitic imidazolate frameworks as Zn2+ modulation layers to enable dendrite-free Zn anodes, Adv. Sci. (2020), 2002173.
- [117] R. Xiao, Z. Cai, R. Zhan, J. Wang, Y. Ou, Z. Yuan, L. Wang, Z. Lu, Y. Sun, Localizing concentrated electrolyte in pore geometry for highly reversible aqueous Zn metal batteries, Chem. Eng. J. 420 (2021), 129642.
- [118] Y. Jiao, F. Li, X. Jin, Q. Lei, L. Li, L. Wang, T. Ye, E. He, J. Wang, H. Chen, Engineering polymer glue towards 90% zinc utilization for 1000 hours to make high-performance Zn-Ion batteries, Adv. Funct. Mater. (2021), 2107652.